Flux pinning dependent quench anomaly in YBCO thin films with stabilizing Au cap layer

Master's thesis
University of Turku
Physics
2026
B.Sc. Umer Zubair
Examiners:
MSc. Samuel Mejia
Dr. Hannu Huhtinen
Prof. Petriina Paturi

The originality of this thesis has been checked in accordance with the University of Turku quality assurance system using Turnitin Originality Check service.

UNIVERSITY OF TURKU
Department of Physics and Astronomy

Zubair, Umer Flux pinning dependent quench anomaly in YBCO thin films with stabilizing Au cap layer

Master's thesis, 59 pp.
Physics
May 2026

High temperature superconductors (HTS) including $YBa_2Cu_3O_{6+x}$ (YBCO)-based coated conductors, have a great potential for application in innovative technologies but these materials pose considerable difficulties due to their instability at high currents and magnetic fields.

This thesis examines the phenomenon of the quench anomaly found in YBCO thin films with stabilizing Au cap layer. The study is aimed at clarifying the underlying mechanism of this problem, focusing on flux pinning and vortex dynamics. Results obtained from AC susceptibility and magnetization transport measurements showed that there is enhancement of flux pinning ability in the presence of BZO doping, especially for high magnetic fields, while reducing the superconducting transition temperature slightly.

Quench experiments were conducted at 65 K under controlled current conditions, where a heat pulse was used to trigger quench events. One of the findings of this study is the existence of a second, delayed voltage peak (quench anomaly) after the initial quench event, once the thermal heat pulse is removed. It has been also observed that BZO doping improves the flux pinning and weakens the quench anomaly peak, whereas higher anomaly peaks observed in the undoped materials can be due to the higher I_c value.

Qualitatively, the observed quench anomaly can be understood by the delay in current distribution between the superconductor and Au stabilizer, among other possible reasons. However, the quench anomaly seems to depend on the flux pinning, external magnetic field, substrate material, and stabilizing capping layer on the top. Overall, this study provides new insights into post-quench instability in HTS materials and highlights the interplay between flux pinning, thermal effects, and current dynamics. These findings are important for improving the reliability and protection strategies of superconducting devices.

Keywords: HTS superconductors, YBCO, BZO doping, flux pinning, quench characteristics, thermal transport, current redistribution

Contents

Preface

This thesis is an effort to provide a better understanding of the superconducting stability of $YBa_2Cu_3O_{6+x}$ (YBCO) thin films. High-temperature superconductors (HTS), especially YBCO-based coated conductors, are considered as an intriguing option for future technologies like superconducting motors, compact wind generators, compact proton therapy systems, and compact fusion power plants. However, the main concern is about their stability and quench protection, which become critically important due to operation under the effect of strong magnetic fields and high currents.

Type-II superconductors such as YBCO exhibit magnetic field vortices that require stabilization through flux pinning. The movement of these vortices leads to energy dissipation causing system instability. During the study of vortex dynamics and pinning behavior, an unusual phenomenon was observed, a delayed second voltage peak following a quench, even after the heat pulse had ceased and the sample regained its superconducting state. This behavior cannot be explained by conventional thermal quench models, indicating that the superconducting state may remain microscopically unstable.

Thesis aims to investigate the cause of the quench anomaly, exploring its relation to flux pinning and vortex reconfiguration. To achieve this, YBCO and BZO-doped YBCO thin films were prepared, grown on two different substrates, and modified with a gold capping layer to understand surface and thermal effects. For this, each sample's critical current (I_c) was measured using the AC transport option of PPMS magnetometer as a function of magnetic field. Quench experiments were then conducted where the transport current was set at 80 percent of I_c for each field. This controlled condition allowed for the study of the vortex system within a strong yet superconducting regime. The voltage response was recorded after applying a heat pulse, leading to a detailed analysis of the first quench peak and the subsequent

anomaly peak. By investigating the behavior of anomalies under different conditions of pinning strengths, substrates, and magnetic fields, this thesis also tries to explore the origins of the delayed voltage peak, positing that it is a result of non-equilibrium vortex dynamics. The findings contribute significantly to the fundamental understanding of superconducting physics and offer critical insights into the operational safety and longevity of HTS devices. Additionally, this research establishes a robust scientific connection between vortex physics and its applications in superconducting technology.

1 Introduction

Resistive heating is a significant issue in current power transmission and technology systems that results in electrical energy losses. They decrease efficiency since much of the energy generated is converted to heat in normal conductors. Superconductivity offers a good solution. Below a certain critical temperature, superconducting materials show zero electrical resistance and perfect diamagnetism. These properties enable effective current transportation and the generation of powerful magnetic fields, making superconductors one of the primary subjects of fundamental research and practice.

Today, superconductors have a wide range of important applications. They are used in the Large Hadron Collider at CERN, where niobium-titanium (NbTi) magnets operate at 1.9 K to accelerate particles at near the speed of light. The superconducting quantum interference devices known as SQUIDs, made with lead, niobium, and YBCO superconductors, detect extremely weak magnetic fields for medical, geological, and defense purposes. MRI machines also use NbTi superconducting magnets to produce precise body scans. However, on the other hand, superconducting cables promise lossless power transmission and Maglev trains in Japan use superconducting magnets for frictionless, high-speed travel. In short, superconductors are not only used for research purposes, but also widely used for commercial applications as well. [1]

High-temperature superconductors (HTSs) have attracted significant scientific and technological interest due to their ability to exhibit superconductivity at relatively higher temperatures. Among them, $YBa_2Cu_3O_{6+x}$ (YBCO) is one of the most extensively studied materials. HTS tapes, also known as second-generation high-temperature superconductor coated conductors (2G HTS CCs), are intriguing options for future technologies like superconducting motors, compact wind generators, compact proton therapy systems, and compact fusion power plants [2]. The

role of flux pinning is crucial in addressing this challenge [3, 4]. In this thesis, we tried to address critical questions related to HTSs, specifically investigate vortex dynamics and pinning behavior in YBCO thin films. It also examines factors such as substrate type, BZO doping, and surface effects that influence superconducting stability. Recent quench experiments on YBCO thin films revealed an anomaly: an unexpected second voltage peak following the removal of a heat pulse, suggesting post-quench instability in a superconducting state. This anomaly indicates that weak or inhomogeneous flux pinning may cause improper vortex confinement, leading to a secondary resistive region and energy dissipation.

This study aims to enhance our understanding of the anomaly related to flux pinning and highlights its importance, contributing to insights into post-quench superconducting instability. This anomaly poses a significant concern in HTSs compared to low-temperature superconductors (LTS). While normal zone propagation velocity (NZPV) in LTS systems is fast (1–10 m/s) and allows for easy quench detection, HTS systems exhibit a much slower NZPV. Consequently, if any hidden instabilities persist after a quench, it indicates that YBCO devices are even more susceptible to catastrophic failures [5].

1.1 Basics of superconductivity

In 1911, Dutch physicist Heike Kamerlingh Onnes made the surprising discovery of superconductivity while examining the electrical resistance of metals at extremely low temperatures [6]. He observed that mercury's resistivity vanished entirely once cooled below about 4.2 K. This phenomenon in which certain materials conduct electric current without electrical resistance, implies that no energy is lost as heat [7, 8].

A major breakthrough was later reported in 1933 by Fritz Walter Meissner and Robert Ochsenfeld who observed that magnetic fields are expelled from supercon-

ductors below a characteristic transition temperature. This phenomenon, known as the Meissner effect, demonstrates that superconductors undergo a phase transition from a normal conducting state to superconducting state, characterized by both zero electrical resistance and perfect diamagnetism [9].

Superconductivity is therefore defined by two fundamental properties: zero electrical resistance and the expulsion of magnetic fields below the critical temperature (T_c). The zero resistance state has been experimentally confirmed through persistent current measurements in superconducting loops, where current flows without measurable decay. This behavior corresponds to an effectively vanishing resistivity, far below that of conventional conductors such as copper ($10^{-8}\,\Omega$m).

Microscopically, superconductivity arises from the formation of Cooper pairs, in which electrons move through the crystal lattice in a correlated state without scattering. This coherent motion suppresses energy dissipation and enables lossless electrical transport. The superconducting state exists only below the critical temperature, which depends strongly on material composition, crystal structure, and impurity content, as defects and impurities can suppress superconductivity [10].

1.1.1 Development of superconductivity theory

The theoretical framework took decades to mature. In 1935, brothers Fritz and Heinz London proposed equations that captured the electromagnetic behavior of superconductors [11]. The London model does not explain the microscopic origin of superconductivity; instead, it only describes its macroscopic behavior. In this model, the electrons are assumed to move in a homogeneous medium and the scattering with the lattice is neglected. As we know that in normal conductors, nuclei are arranged in a lattice, and these freely moving electrons constitute the electric current. These electrons scatter from vibrating lattice ions and impurities, losing energy as heat, which gives rise to electrical resistance. In contrast, in the superconducting state

the electrons effectively do not experience such collisions, and therefore the current flows without losses. The London equations describe the macroscopic behavior of superconductors mathematically. These equations show that the electric field is related to the time-change of the current, which prevents current decay and also helps to explain the magnetic penetration depth and the Meissner effect.

Later, in 1950, Lev Landau and Vitaly Ginzburg created the Ginzburg–Landau (GL) model, which presented practical ideas like coherence length (ξ) and magnetic penetration depth (λ)[12]. They utilized the order parameter (ψ), a complex function related to superconducting electron density to characterize quantum mechanical coherence in the superconducting state. In GL theory, the system favors the lowest free energy, and the free energy functional shows the energy difference between superconducting and normal states. ξ is a spatial fluctuation of the order parameter and λ explains how a magnetic field decays within a superconductor. Based on the ratio λ/ξ, superconductors are classified as type I or type II [8, 11].

Not long after, in 1957, the microscopic BCS theory (named after John Bardeen, Leon Cooper, and John Schrieffer) offered an explanation for the so-called LTS [13]. According to BCS theory, cooling a superconducting material below its critical temperature allows electrons to form Cooper pairs, preventing collisions with nuclei. The Cooper pair is a pair of electrons that is formed at very low temperature. These electrons pair up with each other due to lattice vibrations. Although electrons repel each other due to their negative charge, an attractive interaction occurs when they form Cooper pairs. Cooper pairs behave like bosons, contrasting with the usual fermionic behavior of electrons, enabling them to exist without colliding with nuclei. The formation of Cooper pairs generates an energy gap that must be overcome for the pairs to separate, resulting in a zero resistance current. This phenomenon is attributed to the electron-phonon interaction as described in BCS theory.

A turning point came much later, in 1986, when Georg Bednorz and K. Alex

Müller demonstrated a class of ceramic materials that became superconducting above 30 K [14]. These HTS eventually pushed past 77 K, important because liquid nitrogen is cheap and abundant, which could then replace the costly liquid helium otherwise needed for cooling. This was a major breakthrough because it demonstrated that ceramic copper-oxide compounds could exhibit superconductivity at relatively high temperatures. [8, 14].

1.1.2 Type I and type II superconductors

Superconductors are often divided into two families, depending on how they interact with magnetic fields. Type I superconductors, for instance lead, mercury or tin, possess relatively low transition temperatures (usually under 10 K) and are governed by a single critical magnetic field, beyond which superconductivity disappears abruptly. They lose superconductivity at a critical magnetic field (H_c) and are known as soft superconductors, fully obeying the Meissner effect. Type I superconductors are mostly limited to research and a few low-field applications because they cannot withstand strong magnetic fields. Type II superconductors, in contrast, include metallic alloys and ceramic oxides. They exhibit two critical magnetic fields, H_{c1} and H_{c2}. Below H_{c1}, they behave similarly to type I superconductors and completely expel magnetic flux. Between H_{c1} and H_{c2}, they enter a mixed (vortex) state in which magnetic flux penetrates the material in the form of quantized vortices. These vortices can be pinned by defects or impurities in the material, which suppresses vortex motion and allows the superconductor to sustain higher J_c. Because of this strong flux pinning and the resulting magnetic hysteresis, type II superconductors are often referred to as hard superconductors. Above H_{c2}, superconductivity is destroyed and the material returns to the normal conducting state.This strange allowance for partial field penetration is exactly what makes type II materials so technologically versatile, for instance, in strong electromagnets or

MRI machines [7, 8].

The fundamental distinction between these two classes can be understood through the coherence length ξ and the magnetic penetration depth λ, which together define the Ginzburg–Landau parameter $\kappa = \frac{\xi}{\lambda}$. For type I superconductors, $\kappa < 1$, meaning that the coherence length exceeds the penetration depth. Such behavior is typically observed in relatively pure elemental metals. In contrast, type II superconductors are characterized by $\kappa > 1$, where the penetration depth is larger than the coherence length, a situation most often encountered in alloys and compound superconductors. As a simple comparison, lead behaves as a type I superconductor, whereas niobium-based compounds fall into the type II category.

Another important factor is the surface energy at the boundary between superconducting and normal regions. When this surface energy is positive, the system tends to avoid mixed states, favoring type I superconductivity. On the other hand, negative surface energy stabilizes the formation of vortices and is therefore associated with type II behavior. Although the sign of the surface energy is central to this classification, its influence becomes relatively weak near the superconducting transition temperature.

1.2 YBCO

1.2.1 Structural and superconducting properties

YBCO thin films are widely studied due to their importance in both fundamental superconductivity research and practical technological applications. YBCO is a ceramic superconductor that operates above the boiling point of liquid nitrogen (77 K) with a T_c of approximately 90–92 K [15]. YBCO is regarded as a second-generation HTS and is distinguished by its ceramic oxide nature, placing it within the cuprate family. Its most common stoichiometric representation is $YBa_2Cu_3O_{6+x}$, widely labeled as Y-123. Other structural variants with altered Y:Ba:Cu proportions are

also reported, such as $YBa_2Cu_4O_y$ (Y-124) and $Y_2Ba_4Cu_7O_y$ (Y-247). Although the material has been studied extensively, there is still no single, universally accepted fundamental theory that fully explains high-temperature superconductivity. YBCO's practical viability depends on its capacity to maintain superconductivity under thermal and magnetic stresses, alongside stability and reliability. But the main challenge involves the dynamics of magnetic flux vortices, which is characteristic of type II superconductors like YBCO. Before utilizing YBCO superconductors for practical applications, it is essential to ensure their superconducting properties remain stable under varying temperatures and strong magnetic fields.

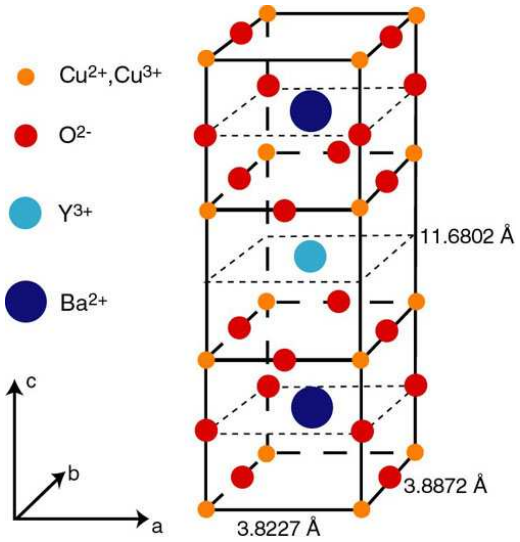

Figure 1: Crystalline structure of orthorhombic unit cell of YBCO [16].

Figure 1 presents the unit cell structure of YBCO. As it can be seen that it is not a perfect perovskite, instead it adopts a distorted perovskite lattice. Its crystal structure is layered in nature, consisting of stacked CuO_2 planes with square-planar coordination that show slight buckling. These CuO_2 planes are primarily responsible for superconductivity. In addition, Cu–O chain layers act as charge reservoirs. Yttrium ions are located between two CuO_2 planes while barium ions occupy positions between the CuO_2 planes and Cu–O chains. This layered structure plays a crucial role in influencing the physical and superconducting properties of

YBCO[17].

The oxygen concentration in YBCO is quite adjustable and it affects the superconducting performance of compound. Although $YBa_2Cu_3O_{6+x}$ is a well-defined chemical phase, it is non-stoichiometric for $0 < x < 1$, meaning the oxygen content varies continuously between 6 and 7 per formula unit. The parameter x represents the additional oxygen content beyond 6. For small values of x (oxygen-poor regime), many oxygen sites in the Cu(1) layer are vacant. In this case, YBCO behaves as an insulator and adopts a tetragonal structure. As x increases toward about 0.65, oxygen atoms progressively occupy the O(1) sites, leading to the formation of Cu–O chains along the b-axis. This oxygen ordering drives a structural transition from tetragonal to orthorhombic symmetry. The lattice constants of the orthorhombic unit cell are $a = 3.82$ Å, $b = 3.89$ Å, and $c = 11.68$ Å. When $x \approx 0.93$, most O(1) sites are occupied, resulting in an optimal hole concentration and strong superconducting properties. The intricate and profound link between composition, structure, and superconductivity in YBCO is demonstrated by the subtle interaction between oxygen ordering and lattice distortion [17].

1.2.2 Doping YBCO with artificial pinning centers

Doping YBCO with artificial pinning centers (APCs), such as BZO nanorods or nanoparticles, introduces defects that enhance vortex pinning and increase the J_c [18]. APCs can be incorporated through *in-situ* growth methods such as co-deposition during PLD or chemical solution deposition, as well as through *ex-situ* mixing of nanoparticles. APCs generally include one-dimensional (1D) nanorods and zero-dimensional (0D) nanoparticles. A common example is BZO in PLD-grown YBCO films, where it self assembles into vertically aligned nanorods along the crystallographic c-axis [19]. These defects create lattice strain, interface disorder, and structural faults that contribute to strong vortex pinning [19, 20].

The effectiveness of APCs is closely linked to the defects and strain fields they produce. BZO has a lattice mismatch of about 7.7 % with YBCO, leading to semi-coherent interfaces that generate dislocations and extended strain fields. Randomly dispersed oxide nanoparticles can also induce Y248-type stacking faults and nanostrain regions, which locally suppress the vortex core energy and improve pinning [20, 21].

The addition of APCs significantly improves J_c and its magnetic-field dependence. Well-aligned BZO nanorods can increase J_c by nearly a factor of three at 40 K compared with poorly aligned structures [19], and they typically produce a pronounced c-axis peak in J_c. The superconducting transition temperature, T_c, is usually only slightly reduced by about 1–2 K [19].

1.3 Quench properties

1.3.1 Basics of quench

A quench is a rapid loss of superconductivity in part of superconductor, causing that region to become resistive. A quench is usually started by a local disturbance in the superconductor, such as a pulse of heat or mechanical motion, leading to a local violation of one or more of the critical limits, resulting in a transition to the normal state [22]. Key factors influencing quenches include the operating current relative to the critical current, the material's heat capacity and thermal conductivity, the amount of metal stabilizer (generally copper) present, and the conductor geometry (e.g. filament or tape architecture) [22, 23]. Normal Zone Propagation Velocity (NZPV) refers to the speed at which a resistive zone, also known as a normal zone, travels along a superconducting wire during a quench process. NZPV plays an important role in the determination of the normal zone and the corresponding voltage.

1.3.2 Quenches in LTS and HTS

The quench initiation and propagation behavior of LTS and HTS are quite distinct due to the differences in LTS and HTS properties. In LTS conductors, the enthalpy margin is small due to their very low operating temperatures, which result in low specific heat and a limited temperature margin to the critical temperature, making them highly sensitive to small energy disturbances[22]. The enthalpy margin represents the amount of thermal energy a superconductor can absorb before transitioning from the superconducting state to the normal resistive state. It is prone to sudden transitions to the normal state. After the quench has started, the normal zone propagates rapidly along the conductor and, in coil configurations, can extend across adjacent turns. This leads to a steep voltage increase, making quenches easier to detect. Due to the inherently high NZPV in LTS conductors, typically in the range of 1–10 m/s, the generated heat is rapidly distributed over a relatively large volume compared to HTS conductors, where heat remains more localized due to much lower NZPV. Therefore, quench heaters are often employed to further spread the energy and prevent localized overheating.

In contrast, the higher enthalpy margin in HTS materials makes them less susceptible to small disturbance. However, in HTS magnets, the quenches tend to be caused by hotspots due to heat loads, microscopic defects, and stress. This resistive zone grows slowly, making quench detection more challenging, particularly in the presence of electromagnetic noise. The low NZPV also leads to larger temperature gradients near the hot spot. Research on HTS magnets, therefore, focuses on enhancing current sharing and stabilization in order to minimize hotspot temperatures. Although this can be achieved by adding more copper in the stabilizer, it results in a loss of current-carrying capacity of the superconductor. In summary, Quenches in LTS magnets occur quickly and are easily detectable, whereas in HTS magnets, they occur slowly and are localized [22].

1.3.3 Impact of quench on various applications

The application of superconductors in industries such as aviation, energy, space, healthcare and quantum technology will have advantages such as saving energy and reducing CO_2 emissions. The effect of quenching is considerable in various applications where stable superconducting magnets are employed. In magnetic resonance imaging (MRI) equipment, the quench results in the fast heating of the system, causing the immediate loss of the liquid helium employed for cooling. It causes the system to shut down, thereby resulting in considerable downtime before the system is re-energized[24]. Furthermore, the abrupt release of energy and gas pressure can cause operational risks and economic consequences. These same issues arise in newly developed superconducting technologies such as fusion magnets, aviation, and high-temperature superconducting power devices. In these devices, a quench can cause a reduction in efficiency. Thus, today's research in quench detection, modeling, and protection strategies play a major role in the safe operation of superconducting systems [25].

1.3.4 Quench detection and protection

Modern quench detection schemes combine classical voltage taps with advanced sensors such as Hall probes, fiber optics, and acoustic methods to identify resistive zones at an early stage, while protection systems employ quench heaters, energy dumping, and novel approaches such as Coupling-Loss-Induced-Quench (CLIQ) to spread or extract energy rapidly. Recent studies highlight the trade-offs involved: voltage-tap thresholds are typically in the range of tens of millivolts with response times of $\lesssim 10\,\mathrm{ms}$ [22], whereas Hall-sensor arrays can detect minute current imbalances of approximately 0.1% of the coil current before any resistive voltage appears [23], and fiber-Bragg gratings (FBGs) in HTS windings can detect single-Kelvin heat pulses with signal-to-noise ratios ranging from 4 to 32 and response times from much less

than 1 s to a few seconds [26]. However, each method has limitations: Hall-based schemes require split or parallel windings and are susceptible to stray magnetic fields, fiber-optic sensors require cryogenically compatible cabling and careful calibration and acoustic emission from the superconducting transition is essentially absent, making passive acoustic monitoring unreliable for quench detection.

Protection strategies include conventional quench heaters, which may suffer from slow thermal diffusion and a risk of electrical shorts, as well as dump resistors or bypass diodes, and more recent approaches such as the CLIQ system, which uses a capacitor discharge to induce rapid coupling losses throughout the coil; when combined with heaters, CLIQ enables a fast and global transition, thereby reducing peak hot-spot temperature [27]. In practice, implementation requires balancing sensitivity against noise and false triggers while accounting for cryogenic wiring and latency constraints: resistive dump circuits can shorten discharge times but are limited by insulation-voltage constraints, and lower detection thresholds increase the risk of false alarms. Consequently, modern quench-protection designs often employ multiple detection channels (e.g. voltage taps together with fiber-optic and Hall sensors) to ensure fast and reliable quench validation while activating robust protection elements such as heaters or CLIQ [22, 23].

2 Methods

2.1 Pulsed laser deposition

Pulsed laser deposition (PLD) is a physical vapor deposition technique widely used to grow thin films, ranging from a few nanometers to several micrometers, on a variety of crystalline and amorphous substrates (Figure 2). In PLD, a short, high-power laser pulse is focused onto a dense solid target (often a sintered or hot-pressed pellet). The absorbed energy leads to rapid material removal (ablation) from the

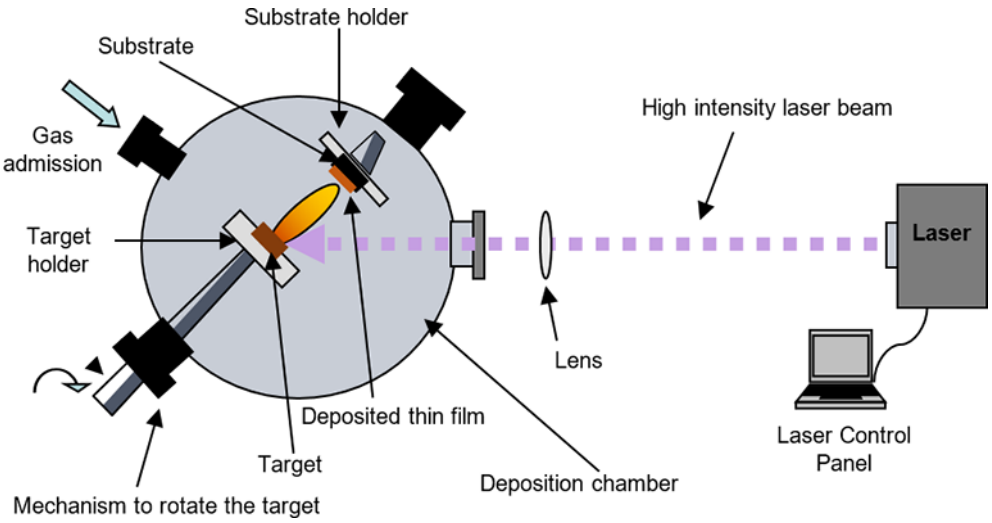

Figure 2: The schematic of PLD process used in this work [31].

target surface and the formation of a highly directed plasma plume containing atoms, ions, and clusters. The plume expands toward the substrate, where the ablated species condense and form a film [28–30].

A key practical advantage of PLD, especially for multicomponent oxides, is the ability, under optimized conditions, to transfer target composition to the growing film with comparatively good stoichiometric fidelity. For oxide films, deposition is commonly carried out in a controlled background gas (e.g. oxygen) to influence plume kinetics and to support correct oxidation during growth [28–30]. Film structure and morphology depend strongly on the growth temperature T_g (substrate temperature during deposition), background-gas pressure/composition, target–substrate distance, and laser parameters such as wavelength, fluence, and repetition rate. Consequently, T_g and the deposition atmosphere were optimized to obtain continuous, uniform films suitable for subsequent patterning and physical-property characterization [28–30].

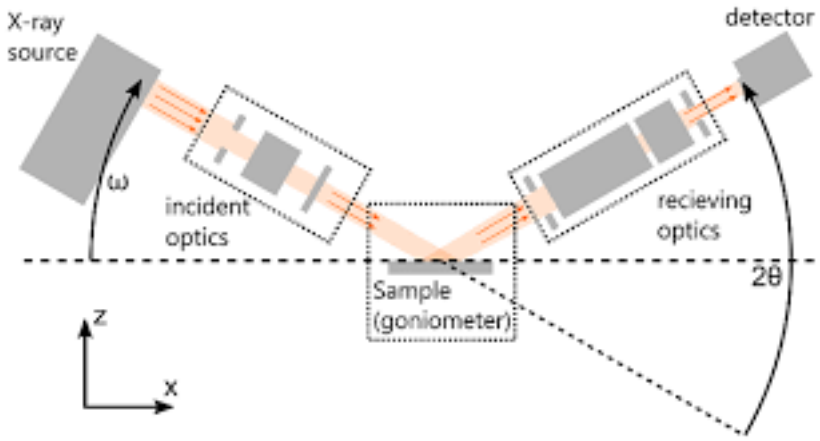

Figure 3: The schematic of XRD process used in this work [33].

2.2 X-ray diffractometry

X-ray diffraction (XRD) was used to characterize film crystallinity, phase formation, and preferred orientation. XRD is based on elastic scattering of x-rays by electrons in the material. Constructive interference of scattered waves from sets of lattice planes leads to diffracted intensity maxima when the Bragg condition is satisfied:

$$n\lambda = 2d\sin\theta,$$

where λ is the x-ray wavelength, d is the lattice-plane spacing, θ is the incident angle relative to the diffracting planes, and n is the diffraction order [32, 33]. Experimentally, diffracted intensity is recorded as a function of scattering angle using a goniometer and detector (Figure 3). Peak positions are used to determine interplanar spacings and lattice parameters, while peak intensities and line shapes provide information on texture and crystalline quality. For thin films, the substrate often contributes strong reflections; therefore, film peaks were identified by comparing measured patterns to expected substrate and film reflections and by tracking systematic changes across samples [32, 33].

2.3 Physical property measurement system (PPMS)

Magnetic measurements were performed using a Quantum Design PPMS system with its AC Measurement System (ACMS II) module. In this setup, a small alternating magnetic field is applied through a primary coil and the sample's response is detected by secondary pickup coils (a mutual-inductance coil design). The output is treated as a complex susceptibility (with in-phase and out-of-phase components), which is very sensitive to superconducting transitions and related relaxation processes. Using this AC-susceptibility data versus temperature, we identified the superconducting transition temperature (marked by the onset of diamagnetic signal) and its width. The ACMS II hardware can also run in a DC magnetization mode by translating the sample through the coils without changing the setup, allowing measurement of static magnetic moments [34].

For transport characterization, we used the PPMS electrical transport options. The AC transport (ACT) mode provided precise current–voltage measurements under controlled temperature and magnetic field (up to 9 T) to determine the sample's critical current using a defined voltage criterion. Resistive transitions and voltage development during high-current quench tests were tracked under various temperature and field conditions [34].

2.4 Photolithography

Photolithography is a standard microfabrication method for transferring geometric patterns into a photosensitive resist and subsequently into an underlying thin film by etching or lift-off. In a typical process flow, the substrate (or film) is cleaned, coated with photoresist by spin coating, soft baked to remove solvent, exposed (mask-based or maskless), developed to form a resist relief pattern, and then the pattern is transferred into the target layer by an appropriate etch chemistry; finally, the resist is stripped [35].

Figure 4: PPMS utilized in this study highlighting the sample chamber, temperature control and measurement probes essential for assessing the magnetic properties of samples across a broad temperature and magnetic field range.

For laboratory-scale rapid prototyping, maskless laser direct writing (LDW) is attractive because it removes the need for a physical photomask and allows direct exposure of resist patterns with digitally defined layouts [36].

To enable controlled quench experiments, we patterned superconducting thin films into microbridge geometries using maskless photolithography followed by wet chemical etching. Samples were cleaned with isopropanol, spin-coated with photoresist at 8000 rpm, and soft baked at 115 °C for 90 s. Patterns were written using a KLOE Dilase laser writer with controlled focus and stage alignment. After exposure, the resist was developed using an alkaline developer (NaOH-based in this work). The exposed film areas were then removed by wet etching in phosphoric acid (H_3PO_4), and the remaining resist was stripped in acetone to yield well-defined superconducting microbridges. Wet etching of YBCO-class cuprate films using phosphoric-acid-based chemistries (as well as alternative complexing etchants such as EDTA) has precedent in prior HTS device processing [35].

2.5 E-beam evaporation

Electron beam evaporation (E-beam) is a sophisticated physical vapor deposition (PVD) process used to produce films that are of high purity and precision. The essential parts of an E-beam evaporator include an electron gun and a crucible. The electron gun produces electrons using a tungsten filament, which glows and then the electrons have sufficient amount of energy to leave. These electrons are then accelerated and focused on the source material with the use of a high voltage electrode. The power level used in the evaporation is controllable with the adjustment of the filament current, which depends on the material. In the crucible, the focused electron beam provides localized heating to the target material, thus causing it to melt and vaporize. The vapor then travels to a substrate, where it condenses to form a thin film layer. The regulation of the process is done by the use of a shutter mechanism, thus providing control over when the material vaporizes and condenses to form the film. This process enables directional deposition for precise texture and film properties [37].

Furthermore, the quartz crystal microbalance (QCM) is also used to observe the deposition rate and the thickness in real-time, which is very essential feedback information in the coating process. The vacuum atmosphere plays a very crucial role as it minimizes the chances of contamination, thus assuring the quality of the films formed. It is worth noting that E-beam is very advantageous in the evaporation of materials with high melting points as the energy is directed to the material only and not the system as a whole [38]. This method has many applications in various sectors, such as electronics, optics, and research, where quality and accurately coated materials exist [39].

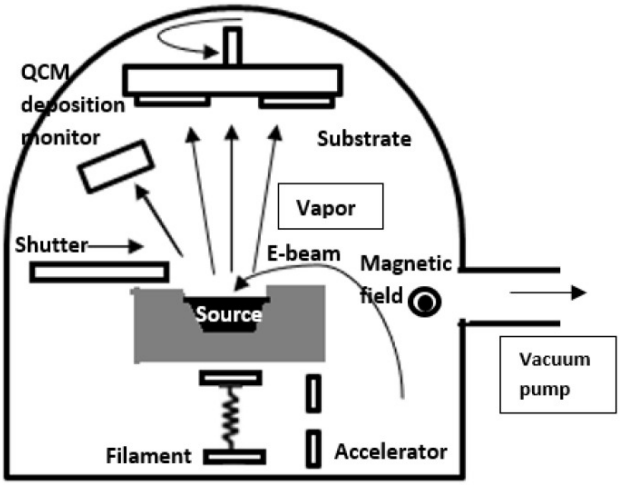

Figure 5: Schematic of E-beam evaporation [39].

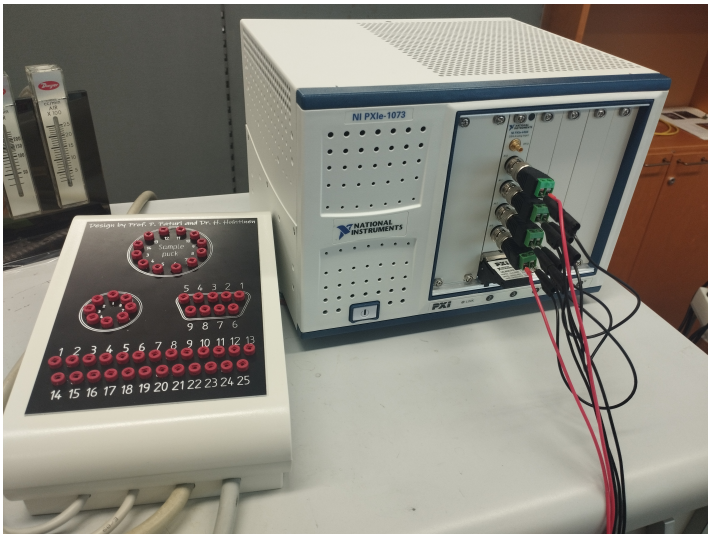

Figure 6: Quench measurement system.

2.6 Quench measurement system

In order to perform quench measurements, we first measured the critical current of the stripe using the ACT option of the PPMS. The sample was mounted on the resistivity puck and a 20 Ω resistor was glued to the stripe to intentionally trigger quench events during quench measurement by providing a heat pulse. It was soldered to thin wires and glued to one end of the superconducting stripe using Stycast epoxy (Loctite Stycast 2850FT with catalyst 23LV). The epoxy was allowed to cure

overnight before the resistor leads were connected to the sample puck. When current flows through this resistor, it locally heats a small region of the stripe, creating a temperature rise that can drive that region into the normal state and initiate quench.

After the electrical contacts with the wire bonder were made, it was inserted into the PPMS sample chamber and connected through a switching box. The purpose of the switching box is to select the sample contacts for applying current and measuring voltage. To verify the connections and the ACT setup, we first measured the stripe resistivity at room temperature (300 K) using a small AC current with an amplitude of 0.1 mA and a frequency of 303 Hz and then sample was cooled to the measurement temperature.

The critical current was determined under magnetic fields ranging from 0 to 8 T by gradually increasing the transport current while monitoring the voltage across the stripe. When the electric field reached the criterion of 1 μV/cm, the corresponding current was recorded as the critical current I_c.

After measuring the I_c values, the PPMS and the measurement instrumentation were set up to perform the quench experiments. The AC transport option is disabled, and the PPMS is restarted with the resistivity measurement option.

A switching box was connected between the PPMS sample chamber and the National Instruments PXIe-1073 data acquisition system (quench measuring device). This switching box allowed us to select which contacts were used for current injection and which were used for voltage measurements. Five voltage taps along the stripe were connected to the quench measuring device using four measurement channels, enabling monitoring of the voltage distribution along the stripe. The quench measuring device was controlled using a computer running a LabVIEW software.

Quench detection measurements were performed using a LabVIEW program that controlled the PPMS current drivers and recorded voltage signals from the taps. For each measurement, a specific current through the stripe is applied based on the

defined I_c value. A heating pulse was then applied to the resistor using a current driver. The pulse sequence consisted of a 200 ms wait-before-current period during which baseline voltages were recorded, followed by a heating pulse of 700 ms.

During the 200 ms waiting period, the quench system recorded the steady baseline voltages from all taps. During the heating pulse, the system recorded the changing voltages along the stripe. If the localized heating was strong enough to drive part of the stripe into the normal state, a quench occurred. In such cases, the quench measuring device detected a sudden increase in the voltages at the taps. These voltage peaks and their timing at different positions along the stripe allowed us to detect the quench event and analyze how the quench propagated along the superconducting stripe.

3 Results and discussion

3.1 Sample preparation

Four 10 × 10 mm^2 thin-film samples were fabricated by pulsed laser deposition (PLD): YBCO/STO, YBCO+4BZO/STO, YBCO/metal, and YBCO+4BZO/metal (Figure 7). After the films were deposited, we patterned them using photolithography. First, a photoresist layer was applied to each sample and then exposed in a laser writer to define the required geometry. The exposed resist was developed using a NaOH solution, and the uncovered film regions were etched with sulfuric acid. This process produced three stripes on every sample.

After patterning, we performed masking to prepare the samples for gold coating, and then deposited Au using e-beam deposition. Each sample contains three stripes with different gold coverage: the first stripe is fully covered with Au, the second stripe has a narrower Au coating on top of it, and the third stripe does not have Au coating. The stripe design follows the layout shown in Figure 8, where there are two

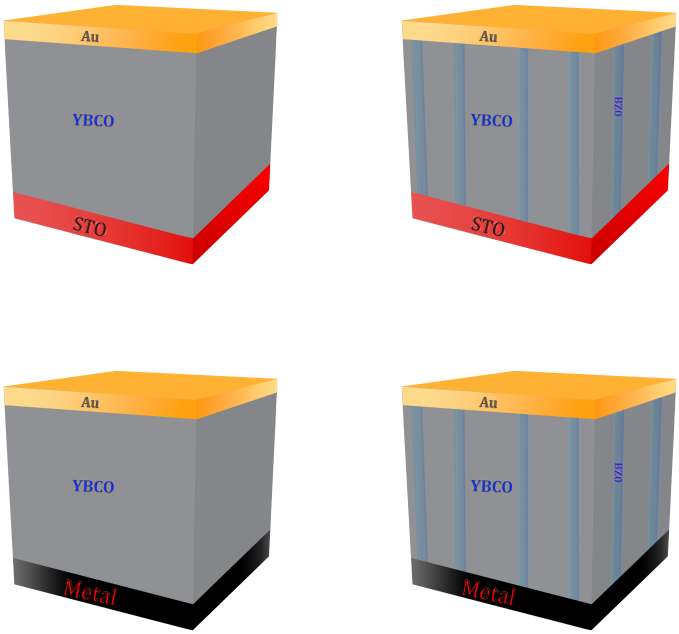

Figure 7: Schematic illustration of YBCO thin films on different substrates with and without BZO pinning centers. The upper pair represents films grown on an STO substrate, while the lower pair corresponds to films on a metal substrate. In each pair, one sample is without BZO and the other includes BZO nanorods as artificial pinning centers.

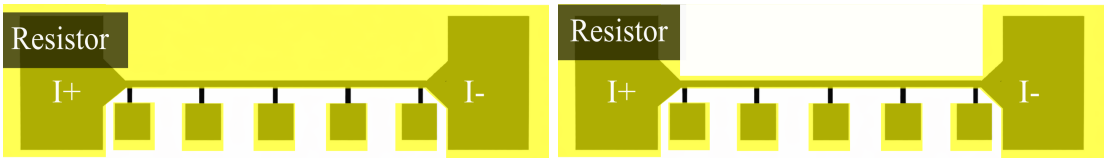

Figure 8: Illustration of a stripes fully (left) and narrowly (right) coated with Au, where the spacing between adjacent channels is 1 mm.

main current paths and five voltage channels positioned between them for quench measurements.

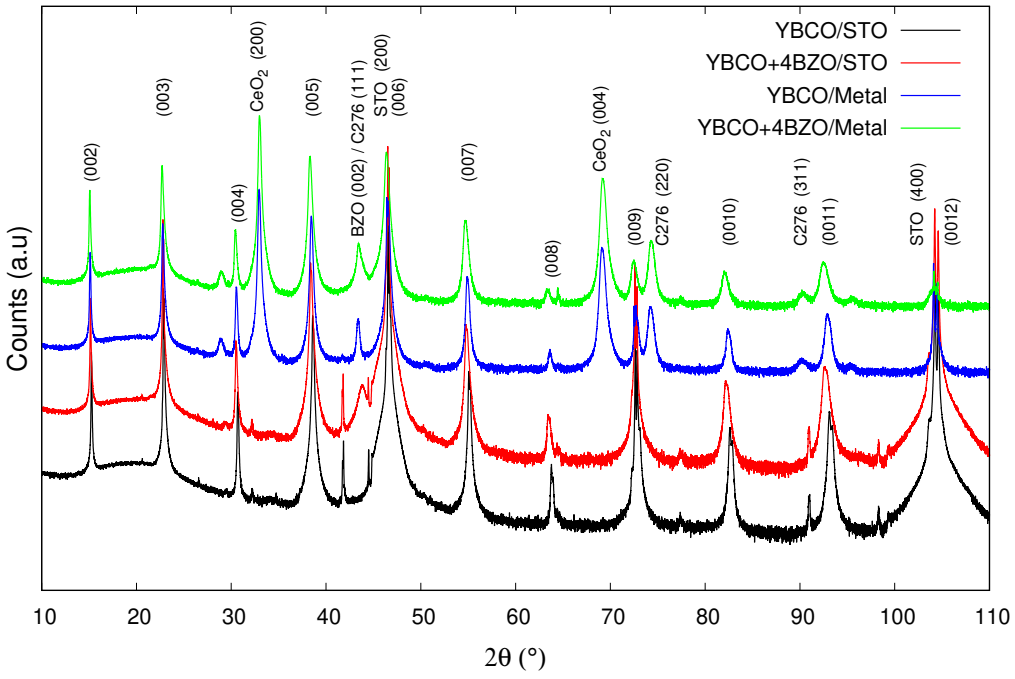

Figure 9: The full 2θ-scan of all samples. Peaks have been labeled according to their source.

3.2 Structural properties of films

3.2.1 X-ray diffraction analysis

To investigate the crystallinity of YBCO films, XRD measurements were performed, and the 2θ scan of all samples are shown in Figure 9. The 2θ-scan measurements of the (005) diffraction peak for four samples reveal significant variations in crystalline quality and lattice strain characteristics. The XRD measurement results are better at medium θ angles, this is one of the reasons we focus on the (005) peaks. Another reason for choosing (005) peak is that they have highest intensity and do not overlap with the STO peaks. As can be seen in Figure 10, YBCO/STO film has the most intense and narrowest peak, which indicates superior crystalline order, excellent c-axis epitaxial alignment, and the lowest lattice strain. The addition of BZO nanoinclusions causes a modest broadening of the peak and a reduction in intensity, which indicates increased lattice strain and extra distortions. Films grown on

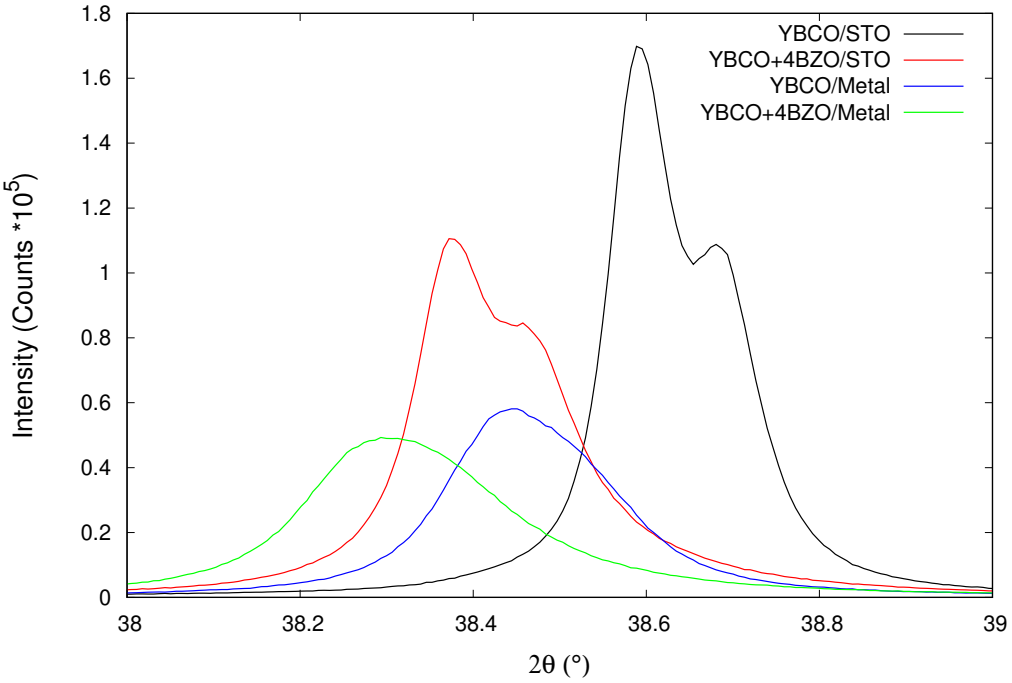

Figure 10: 2θ-scan results focused on the (005) peaks show clear peak widening and shifting in the presence of BZO nanorods.

metallic substrates show greater peak broadening and intensity reduction, indicating substantial lattice mismatch, increased microstrain and degraded out-of-plane alignment. The YBCO+4BZO/Metal has the broadest and weakest peak, indicating the lowest crystalline quality. These observations establish that STO substrates offer superior lattice matching and epitaxial stability compared to metallic substrates, while BZO doping introduces controllable nanoscale strain fields that moderately affect but do not eliminate the epitaxial integrity of YBCO thin films.

Substrate induced strain within the crystal lattice can lead to defects and adversely affect epitaxial growth. In our samples, there are two primary sources of strain: the first one is the lattice mismatch between the substrate unit cells and the unit cells of YBCO and BZO, and the second is the lattice mismatch between YBCO and BZO. We studied these strain values through Williamson–Hall (WH) analysis

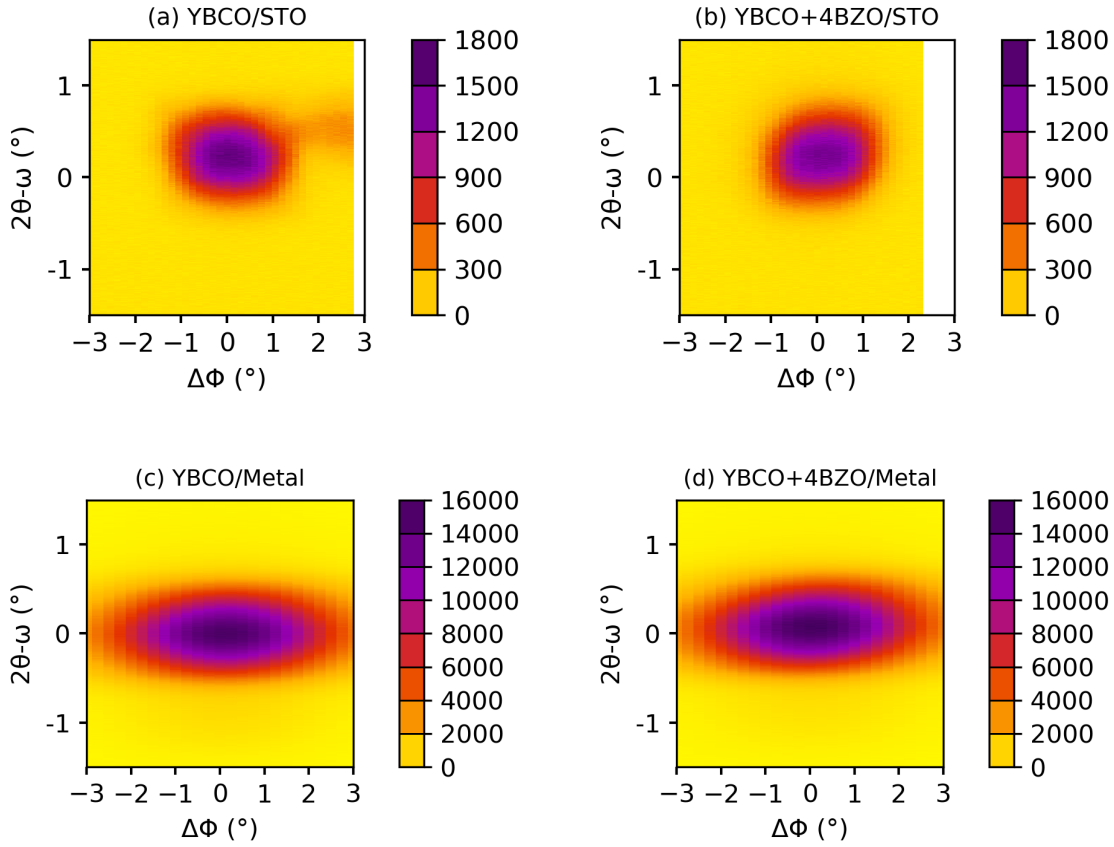

Figure 11: Intensity (counts) is shown as a function of the azimuthal angle ϕ and the diffraction angle 2θ. The multilayer samples exhibit higher intensity maxima, indicating more prominent peaks and consequently enhanced in-plane characteristics.

by examining the peak widths in the 2θ scans. The Williamson–Hall relation is

$$\beta \cos\theta = \frac{k\lambda}{D} + 4\varepsilon \sin\theta, \tag{1}$$

where β is the full width half maximum (FWHM) in radians, θ is the Bragg angle, k is the shape factor, λ is the x-ray wavelength, D is the crystalline size, and ε is the microstrain (WH strain). The results are shown in table I.

In-plane orientation was analyzed using the ϕ-scan of the (102) reflection, revealing that YBCO/STO and YBCO+4BZO/STO have a $\Delta\phi$ of around 2°, while metal-template films exceed 4°, suggesting weak epitaxy. ϕ-scan measurements also

tell us about epitaxial relationship of YBCO thin films deposited on two different substrates, both with and without BZO nanoinclusions. As can be seen in Figure 11, the pristine YBCO/STO film shows a symmetric and relatively narrow peak in the ϕ-direction, indicating good in-plane crystalline alignment. This indicates low mosaicity and minimal lattice distortion, indicating a well-matched lattice environment for high-quality YBCO film growth. The YBCO+4BZO/STO sample exhibits a moderate increase in mosaic spread due to BZO nanoparticle inclusion, which may aid in strain relaxation while maintaining structural coherence between the YBCO film and the STO substrate.

However, YBCO films on metallic substrates showed broader, less intense ϕ-peaks, indicating greater in-plane misalignment, elevated strain, and enhanced lattice distortion compared to STO-based counterparts. The YBCO+4BZO/Metal sample displayed the broadest and weakest ϕ-scan signal, suggesting substantial deterioration in crystalline texture and epitaxial quality. In conclusion, ϕ-scan confirms that STO substrate has superior in-plane epitaxial alignment, while metallic substrates induce significant structural disorder and the inclusion of BZO slightly modifies the strain without completely disrupting the epitaxial alignment.

Figure 12 shows the rocking curves of four different samples. The rocking-curve measurements (ω-scan) provide insights into out-of-plane alignment by measuring the tilt of crystal planes relative to the substrate surface. A narrow peak indicates good alignment, while a broad peak indicates poor alignment. The YBCO/STO sample shows the narrowest rocking curve width ($\Delta\omega_{005}$=0.37°), whereas metal template samples exhibit widths of approximately 1.5°, indicating greater mosaic spread. The YBCO/STO film displays a sharp peak with the smallest FWHM, indicating excellent c-axis alignment and high crystalline perfection. This narrow rocking curve confirms that the film has minimal lattice distortion and very low dislocation density, highlighting the strong epitaxial match between the YBCO layer

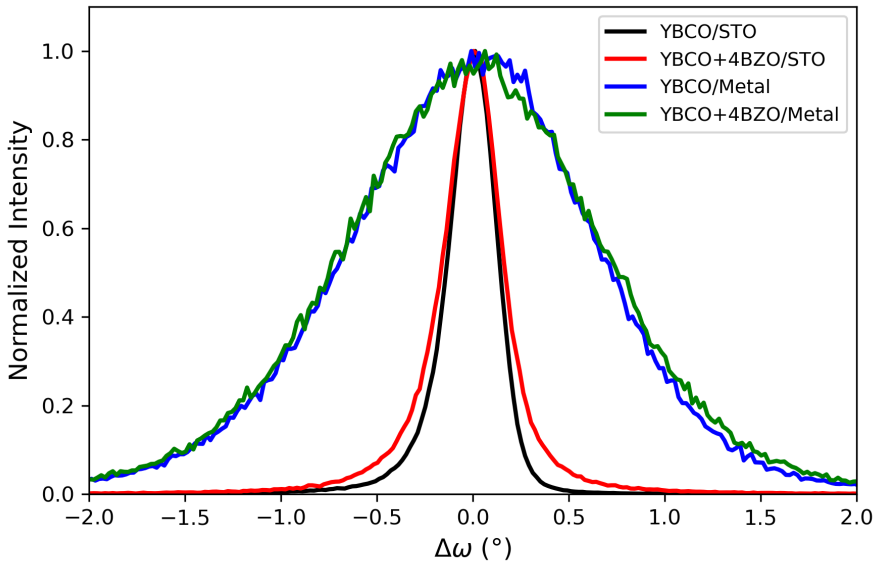

Figure 12: Rocking curve results for the (005) peaks of all samples. The data have been normalized to allow for direct comparison of peak shapes and widths. The variation in peak width is clearly observable providing insight into the crystalline quality and alignment of the samples.

and the STO substrate. This also reveals that the incorporation of BZO nanoinclusions into YBCO/STO leads to a slightly broader ω-peak, indicating localized strain fields and minor lattice tilts. However, the overall c-axis orientation remains unchanged, suggesting that moderate BZO incorporation only modestly impacts the film's crystalline order and does not significantly disrupt epitaxial growth on STO.

YBCO films grown on metallic substrates show a significant reduction in crystalline quality, with broader and weaker ω-scan peaks, indicating increased mosaic spread, grain misorientation, and structural disorder. The YBCO+4BZO/Metal sample has the broadest profile indicating the highest degree of out-of-plane lattice distortion. The results of the $\Delta\omega$ values, together with all XRD results in other directions, are compiled in Table I. The intensity ratios $I(005)/I(004)$ reflect the oxygen content within the samples[40]. The maximum ratio of 16.6 was observed for YBCO+4BZO/STO, indicating slightly less oxygenation compared to YBCO/STO.

Table I: Comparison of crystallographic properties of the undoped and BZO-doped YBCO samples deposited on STO and buffered metal substrates.

Sample	$\Delta\theta$ (005) [°]	$\Delta\phi$ (102) [°]	$\Delta\omega$ (005) [°]	$I(005)/I(004)$	$\varepsilon_{\mathrm{WH}}$ (%)
YBCO/STO	0.101	1.980	0.301	15.297	0.085
YBCO+4BZO/STO	0.140	1.899	0.365	16.611	0.195
YBCO/Metal	0.181	4.175	1.515	13.677	0.149
YBCO+4BZO/Metal	0.241	4.118	1.593	15.927	0.285

Table II: Lattice parameters.

Sample	a [Å]	b [Å]	c [Å]
YBCO/STO	3.854	3.859	11.655
YBCO+4BZO/STO	3.844	3.861	11.716
YBCO/Metal	3.702	3.817	11.701
YBCO+4BZO/Metal	3.684	3.816	11.744

The ratio for metal-template films lies between 14 and 16.

Lattice-parameter analysis (Table II) shows that films grown on metal substrates exhibit smaller in-plane a and b parameters, measured as a=3.684 Å and b=3.816 Å for YBCO+4BZO/Metal. In contrast, the c-axis elongates to approximately 11.74 Å, indicating a normal response to in-plane compressive strain and BZO inclusions.

Overall, XRD results demonstrate that films grown on STO substrates exhibit superior structural quality with the least amount of strain. In metal templates, greater lattice mismatch results in broader diffraction peaks and increased strain, while BZO nanoinclusions enhance the non-uniform strain without significantly affecting the c-axis. This emphasizes that the choice of substrate is the most critical factor in controlling crystalline quality, which again has a direct impact on the flux pinning properties.

3.3 Magnetic characterizations

3.3.1 Ac susceptibility measurements

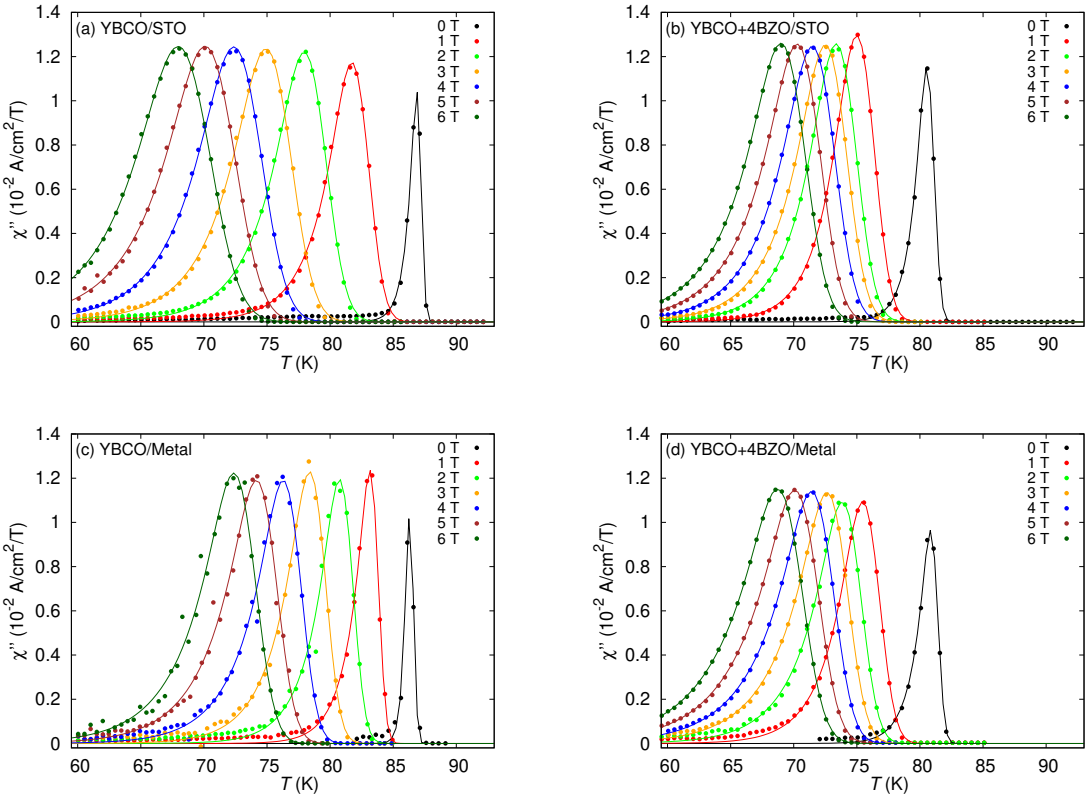

Figure 13: Imaginary part of magnetic susceptibility (χ'') for YBCO/STO superconducting samples under different magnetic fields. The χ'' component represents energy dissipation within the material. The peaks were fitted using an exponentially modified Gaussian (EMG) function to determine the temperature of the maximum and the peak width.

The imaginary part of AC susceptibility (χ'') measures how much energy a superconductor loses, which comes mainly from moving magnetic vortices in the material. In AC experiments, the peak in χ'' versus temperature roughly marks the transition temperature where the superconductor starts to lose its resistance, and this peak corresponds to maximal energy dissipation from vortices. In order to better understand, the $\chi''(T)$ peaks were fitted using an exponentially modified Gaussian (EMG)

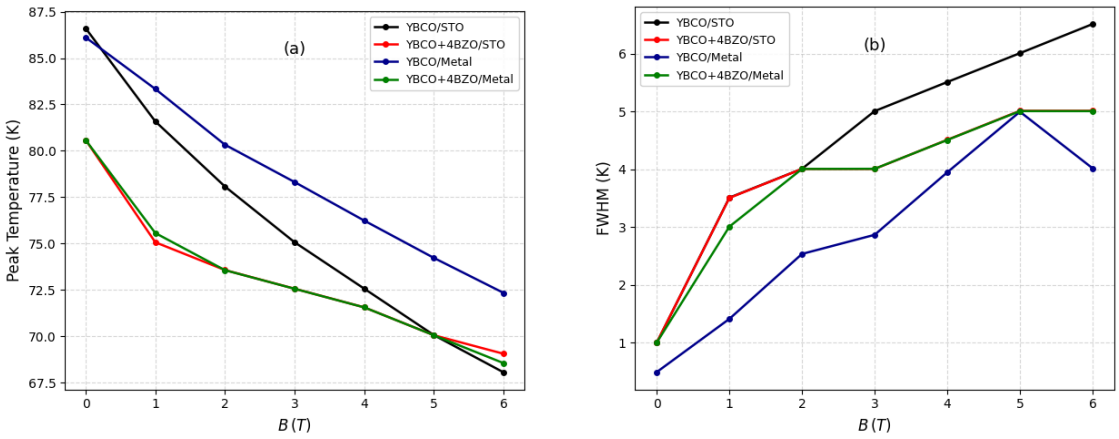

Figure 14: Magnetic field dependencies of the χ'' peak maximum $T_{\max}$ (a), and the FWHM of the χ'' peak (b).

function to account for their asymmetric shape. The fitting function is given by:

$$f(T) = \frac{A}{2\tau} \exp\left(\frac{\sigma^2}{2\tau^2} - \frac{T_{\max} - T}{\tau}\right) \operatorname{erfc}\left[\frac{1}{\sqrt{2}}\left(\frac{\sigma}{\tau} - \frac{T_{\max} - T}{\sigma}\right)\right]. \tag{2}$$

Here, A is the amplitude, $T_{\max}$ is the peak position obtained from the maximum of the fitted curve, σ represents the Gaussian broadening related to the full width at half maximum (FWHM) of the peak. The shape of this peak (its position, width, and height) tells us about vortex behavior and pinning. For example, a tall, narrow peak usually means the film is very uniform with strong vortex pinning (high crystalline quality), whereas a broad peak indicates weaker pinning and more vortex motion. When an external magnetic field is applied, this peak shifts to lower temperature and often broadens, showing that the field weakens superconductivity and makes vortex motion easier [41, 42].

In the YBCO/STO film, the χ'' curve shows a sharp peak around $86, \mathrm{K}$ in zero field. As the magnetic field is increased up to $6, \mathrm{T}$, this peak moves steadily to lower temperature (T_c drops) but remains well-defined. Figure 14b shows a measurable increase in FWHM with increasing magnetic field, indicating enhanced vortex motion and dissipation under applied field. Nevertheless, the superconducting transition

remains distinct, suggesting relatively uniform current flow and good crystalline quality of the epitaxial film grown on the STO substrate. By contrast, films on metal substrates often contain more roughness and grain boundaries, which can weaken the superconducting properties [43].

For the YBCO+4BZO/STO film, the zero-field χ'' peak is found at a somewhat lower temperature (around 80 K), but it is still sharp. As the field increases, the peak shifts to the left (T_c decreases), indicating the expected suppression by the magnetic field. However, unlike the undoped film, the transition remains relatively well defined even at high magnetic fields. This means the BZO nanorods are acting as very effective pinning centers. They trap and immobilize the magnetic vortices, reducing their motion and thus keeping energy losses low at high fields [44, 45]. In other words, adding BZO greatly strengthens flux pinning: it stabilizes the vortices and suppresses flux creep. This is consistent with previous studies showing that YBCO films with BZO nanocolumns exhibit much stronger pinning and maintain superconductivity to higher fields than pure YBCO. (Indeed, one study found an optimal BZO content around 8–10 percent gives the best pinning and highest critical currents) [44, 45]. Because of the strong pinning, the transition in the BZO-doped film remains sharp under field and energy dissipation stays lower, confirming that the BZO-enhanced film has more stable vortex behavior in applied fields.

In contrast, the YBCO/Metal film (YBCO on a buffered polycrystalline metal template) shows a different response. Its χ'' peak at $0, \mathrm{T}$ is again near $86, \mathrm{K}$. As the magnetic field increases, the peak temperature shifts rapidly toward lower temperatures, indicating a stronger suppression of superconductivity compared to the YBCO/STO film. Although the FWHM values in Figure 14b remain lower than those of the YBCO/STO sample, the strong peak shift suggests reduced vortex stability under applied magnetic field. The metallic substrate introduces imperfections such as grain boundaries, surface roughness, and mismatch defects, which break up

the film into less uniform regions. These imperfections act as "weak links" and limit superconducting current flow. As a result, the superconducting properties of the film are more sensitive to the applied magnetic field.

When 4% BZO is added to the YBCO/Metal film, its behavior improves significantly. The zero-field χ'' peak shifts down to about 80 K, but as the field increases the peak moves to lower temperature much more slowly than in the undoped YBCO on metal substrate. The peaks also remain relatively sharp. In other words, the BZO nanorods again serve as strong pinning centers even on the metal substrate. They trap vortices and prevent them from moving freely, which reduces AC losses under field. This leads to a superconducting state that is more stable in magnetic field than the undoped metal film. The smaller peak shift and narrower width in the BZO-doped YBCO film on metal confirm that its flux pinning and vortex stability are greatly enhanced by the BZO nanorods.

Overall, these observations show that both the choice of substrate and the addition of BZO determine the film's performance. Single-crystal STO substrates yield the highest T_c and the cleanest transitions due to uniform epitaxy, whereas metal substrates typically show more field-sensitive superconducting behavior because of structural imperfections [43]. Adding BZO nanoparticles consistently improves flux pinning, at the cost of a modest reduction in zero-field T_c (as seen by the peaks 80 K) due to strain or disorder from the second phase. This tradeoff is worthwhile: with BZO, the films retain their superconductivity to higher fields and exhibit sharper transitions than without APCs. In fact, research has found that combining one-dimensional pinning centers (like BZO nanorods) with three-dimensional nanoscale defects generally produces the best superconducting properties [42]. In our case, the best balance appears in the YBCO+4BZO films on both STO and metal substrates. These trends agree with past studies that emphasize how optimizing both the film's structure and its pinning landscape is key to achieving high performance in YBCO

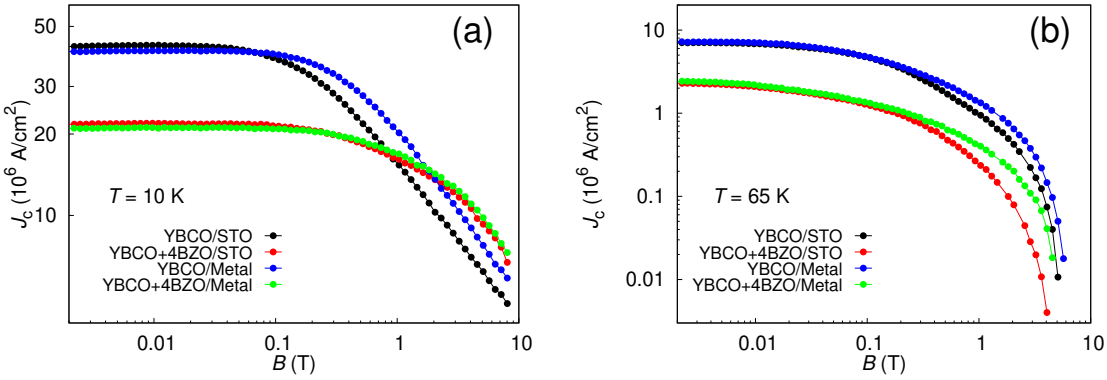

Figure 15: Magnetic field dependence of J_c for all four samples measured at (a) 10 K and (b) 65 K.

superconductors [42, 45].

3.3.2 Magnetic field dependent critical current densities

The magnetic field dependence of J_c reveals a clear influence of BZO doping at different temperatures, as we can see from Figure 15. At 10 K, the undoped YBCO sample exhibits higher J_c in the low-field region indicating that intrinsic pinning is sufficient under these conditions. However, with increasing magnetic field, a crossover behavior is observed where the BZO-doped samples outperform the undoped one and maintaining higher J_c at high fields. This improvement is attributed to the enhanced flux pinning introduced by BZO nanorods, which effectively immobilize vortices under strong magnetic fields.

In contrast, at 65 K, thermal fluctuations weaken the pinning efficiency, reducing the overall J_c for all samples. Under these conditions, the advantage of BZO doping becomes less pronounced, and the undoped sample can exhibit comparatively higher J_c, particularly at low to moderate magnetic fields. It is likely that, to clearly observe the beneficial effects of BZO doping at 65 K, measurements would need to be extended to even higher magnetic fields, where enhanced pinning could become more significant. Overall, the results demonstrate that BZO doping significantly enhances

high-field performance at low temperatures, while its effectiveness diminishes at elevated temperatures due to reduced pinning strength. It is worth noting that quench measurements at 10 K were not conducted due to various reasons. At 10 K, the values of I_c are too high and beyond the capacity of the setup, which can only handle a maximum current of 1 A. In order to handle high values of I_c, the cross-sectional area would have to be reduced for the superconducting stripe. However, such modifications were not feasible within laboratory constraints. In addition, increasing the current poses a high risk of damaging the superconducting stripe, which would compromise the integrity of the sample.

3.4 Quench and its anomaly measurements

3.4.1 Critical current values employed in the measurement

I_c values of all the samples, have been extracted from AC transport measurements as a function of magnetic field, which are presented in this section separately for the samples with wide and narrow Au coatings. For the quench and its anomaly experiments, the transport current was kept at 80 percent of the I_c value that had been measured at each field. This ensured that the samples would remain in a superconducting state but still close to the critical limit, thereby allowing a quench to be initiated under controlled conditions by the heat pulse.

For the samples on STO with a wide Au coating shown in Figure 16(a), it can be observed that for both YBCO/STO and YBCO+4BZO/STO, there is a definite trend of decreased I_c with increasing magnetic field at 65 K. The YBCO/STO sample shows higher values of I_c over the entire range of the applied magnetic field, especially at lower values of the applied magnetic field. At higher values of the applied magnetic field, the values of I_c for both samples are decreased, showing a lower difference between the two.

Similar kinds of behavior are seen for the metal-based samples too (Figure 16(b)),

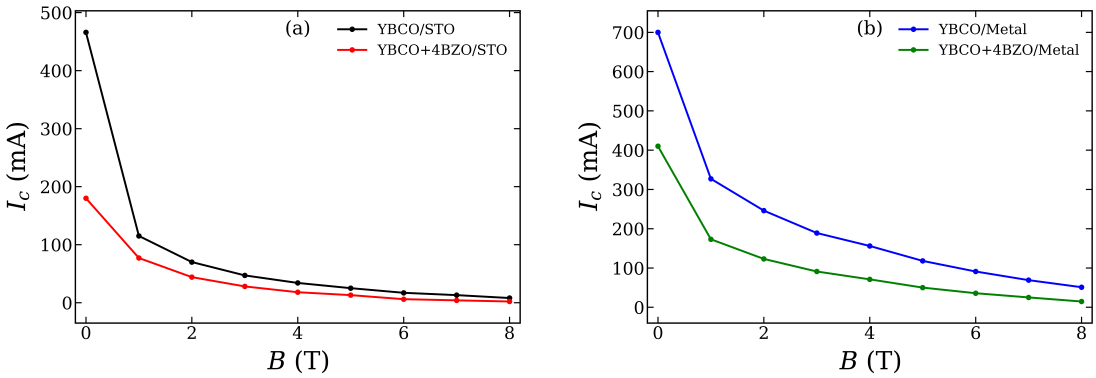

Figure 16: I_c vs B for (a) STO and (b) metal samples with wide Au coating at 65 K.

where YBCO/Metal as well as YBCO+4BZO/Metal have shown a similar trend of decreasing I_c values with increasing magnetic field. For the YBCO/Metal sample, higher values of I_c are seen, especially at low magnetic fields; the difference between the values for these two kinds of samples is more prominent. At higher magnetic field values, the I_c values for these two samples are closer to each other, indicating the impact of BZO doping at higher magnetic field values.

Figure 17(a)-(b) illustrates the magnetic field dependence of I_c for STO- and metal-based samples with a narrow Au coating. In all cases, I_c decreases with an increase in magnetic field. In the case of STO-based samples, YBCO/STO has higher I_c values, especially at low magnetic fields, compared to YBCO+4BZO/STO, with the difference between them being more prominent, whereas at higher magnetic fields, their I_c values become comparable. A similar trend has been observed for metal-based samples, with YBCO/Metal having higher I_c values at low magnetic fields, whereas the difference between them and YBCO+4BZO/Metal reduces at higher magnetic fields, with their I_c values becoming comparable.

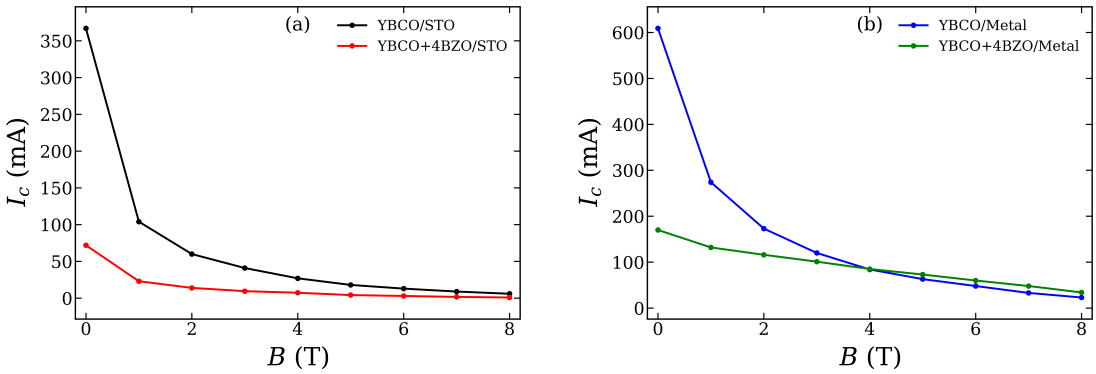

Figure 17: I_c vs B for (a) STO and (b) metal samples with narrow Au coating at 65 K.

3.4.2 Optimizing the heat pulse to obtain the quench

Figure 18 presents the time evolution of the voltage signal for all four samples with wide Au coating under a fixed magnetic field of 3 T, demonstrating the optimization of the heat pulse necessary for a reliable quenching process. The heat pulse causes a transition from the superconducting state to the resistive state, as indicated by the voltage rise.

In both panels, it is evident that the voltage is near zero prior to the heat pulse, demonstrating that the samples are in a superconducting state. After the heat pulse is applied, a sharp increase in voltage is seen, indicating the creation of a normal state in the superconducting stripe. This first peak is the main quenching event caused by localized heating.

A significant difference in quench characteristics can be seen between the samples grown on STO substrates and metal templates. Figure 18(a) shows that the undoped YBCO/STO sample exhibits a higher voltage peak compared to the YBCO+4BZO/STO sample. The decrease in the voltage peak of the YBCO+4BZO/STO sample suggests improved in-field stability, which may be associated with enhanced flux pinning that suppresses vortex motion and reduces energy dissipation. How-

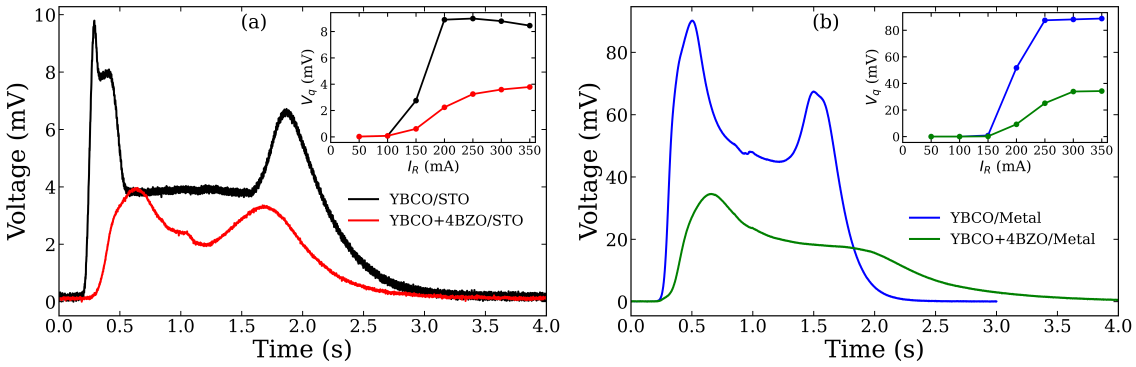

Figure 18: Time evolution of voltage measured at 3 T at 65 K for films on (a) STO and (b) metal substrates with wide Au coating, comparing quench peak. Insets show peak voltage vs applied resistor current, increasing with heat pulse.

ever, this reduction may also be influenced by differences in the absolute current values, and therefore both effects should be considered. Figure 18(b) demonstrates higher voltage peaks for the metal-based samples, with the YBCO/Metal sample having a voltage peak of around 78.6 mV. This demonstrates an abrupt quenching process. This behavior may be related to the inferior crystallinity, higher defect density, and reduced flux pinning properties associated with the metal-based templates. However, the possibility that higher current levels contribute to the rapid quenching cannot be excluded, and the observed response is likely influenced by combination of these factors. In the BZO-doped metal sample, the voltage peak is reduced to around 33 mV, reinforcing the positive effects of BZO on vortex pinning and superconducting stability even for structurally inferior films.

In both Figures 18(a) and (b), the insets show how the peak voltage of the quench depends on the applied current through resistor. It can be seen that as the applied current increases, the peak voltage also increases monotonically, indicating that a larger temperature perturbation leads to a higher quench peak voltage, thus confirming our assumption that the applied heat pulse is the major cause of the quench effect. It should also be noted that at a resistor current of 350 mA, both

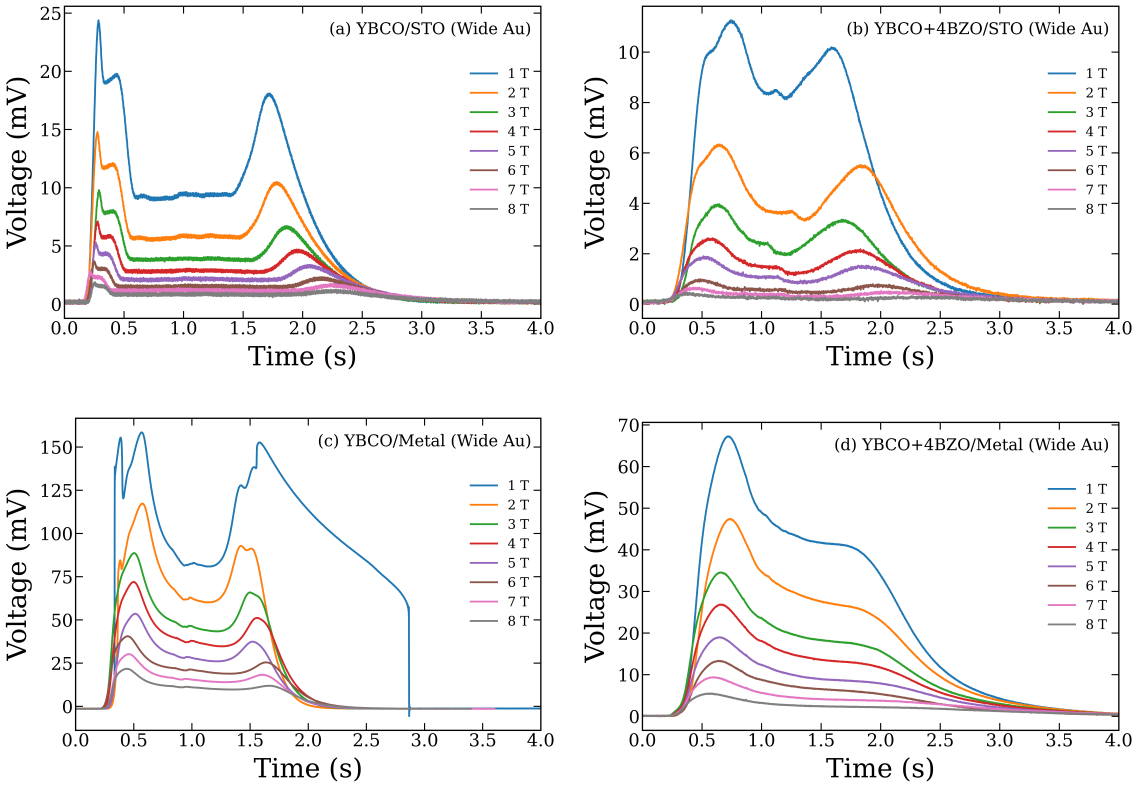

Figure 19: Magnetic field dependence of time-dependent quench behavior in wide Au-capped films measured at 65 K, for fields from 0 to 8 T, showing variations in quench dynamics and emerging anomalies.

primary quench peak and anomaly peak are well observed in all samples. This further indicates that the heat pulse applied to the sample in the experiment at a current of 350 mA is adequate to trigger both quenching and anomaly. Thus, in order to ensure consistency in all measurements in this study, all quench current measurements were made at a constant resistor current of 350 mA. On the whole, it is seen that the results validate the appropriateness of the heat pulse parameter values selected for this study in terms of ensuring a controlled and reproducible quench in all samples.

3.4.3 Magnetic field dependence of quench and its anomaly in widely Au-capped films

From the time-dependent quench measurements in Figure 19, we can clearly observe that in all cases two specific features of the quench behavior are observed: the main quench peak, which is observed immediately after the heat pulse is applied, and the second peak, which is observed later, here called an anomaly peak. It is clearly seen that the voltage response for STO-based samples, i.e., for the YBCO/STO and YBCO+4BZO/STO samples, is clearly defined and smooth in all cases of the magnetic field. At low magnetic fields, a strong quench peak and a clearly distinguishable anomaly peak are observed. With increasing field values, there is a decrease in peak height and reduction in anomaly magnitude, but there is always a temporal distinction between the two peaks. There is a strong quench and anomaly peak in the YBCO/STO sample compared to the YBCO+4BZO/STO sample, especially when the field is lower; however, there is an observable delay before the occurrence of the anomaly, implying a relaxation mechanism.

In the case of the metal-based samples in Figure 19(c) and (d), a clear distinction is seen between the undoped YBCO/Metal and the BZO-doped YBCO+4BZO/Metal samples. In the YBCO/Metal sample, extremely high voltage peaks are observed, especially at low magnetic fields. At low magnetic fields, two closely spaced quench peaks are first observed. This is then followed by a slight drop in voltage, and then a wide anomaly peak appears, especially at 0 and 1 T, also the anomaly peak has multiple shoulders, which implies a non-uniform and multi-stage voltage evolution. Moreover, the voltage does not decay smoothly, and it has a long tail, which indicates a long period of dissipation and a non-uniform recovery of the superconducting state. At higher applied magnetic fields, the quench peaks and the anomaly peak become smoother and simpler, having lower peak heights and fewer irregularities, which indicate a stable behavior. Overall, this behavior suggests significant inhomo-

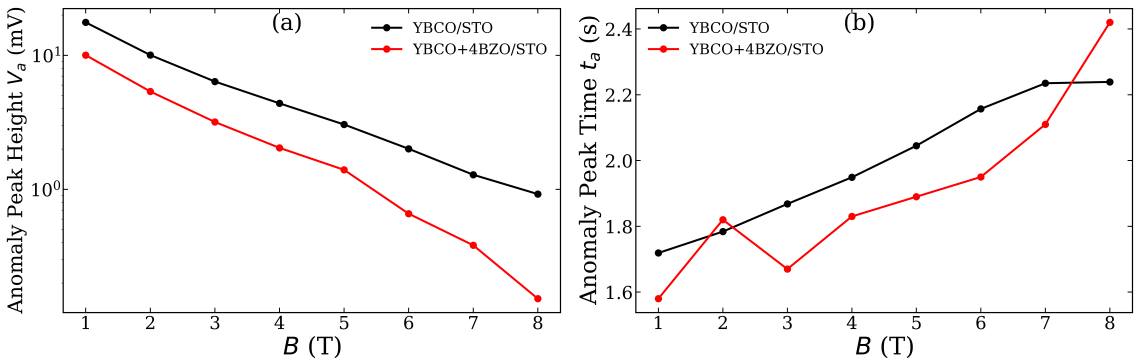

Figure 20: Magnetic field dependence of the anomaly peak height (a) and anomaly peak time (b) for YBCO/STO and YBCO+4BZO/STO films.

geneity in current distribution and weaker flux pinning, allowing vortices to move more freely, particularly at low magnetic fields.

On the contrary, the voltage response curve of the YBCO+4BZO/Metal sample has a more controlled voltage response with reduced peak heights in all the magnetic field values. After the initial quench peak, the sample has a less distinguishable anomaly peak, which resembles a shoulder on the decaying voltage curve rather than a distinguishable peak as in the undoped sample. This shoulder-like feature still points to the detection of an anomaly, but its reduced intensity points to a suppression of vortex motion as a result of improved flux pinning. The voltage curves also display a smoother and more gradual decay. This is sign of reduced dissipation and a more homogeneous recovery of the superconducting state.

For the STO-based samples presented in Figure 20, the magnetic field dependence of the anomaly peak height and the anomaly peak time is observed. In Figure 20(a), the anomaly peak height decreases with increasing magnetic field for both samples. At a given field and under the same applied current, the undoped YBCO/STO sample exhibits a consistently higher peak voltage than the YBCO+4BZO/STO sample. This indicates stronger dissipation in the undoped sample, arising from weaker flux pinning and enhanced vortex motion. In contrast, the reduced peak

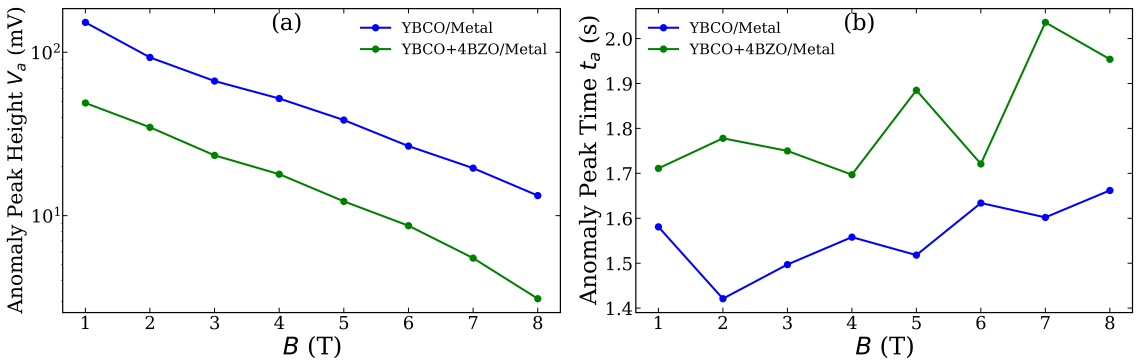

Figure 21: Magnetic field dependence of (a) anomaly peak height and (b) anomaly peak time for YBCO/Metal and YBCO+4BZO/Metal samples.

height in the BZO-doped sample confirms that BZO incorporation improves flux pinning, thereby suppressing vortex motion and associated energy dissipation.

The anomaly peak time (Figure 20(b)), on the other hand, reveals a different trend from the peak height. In the case of the YBCO/STO sample, the peak time decreases at lower magnetic fields and then starts to increase as the magnetic field increases. This implies a change from faster to slower dynamics in the vortex relaxation process. In the YBCO+4BZO/STO sample, the peak time remains lower and fluctuates less at lower magnetic fields, but the increase at higher magnetic fields is significant. This implies that the stronger pinning makes the process more controlled but slightly delayed.

For metal-based samples, as shown in Figure 21(a), the anomaly peak height decreases with increasing applied magnetic field for both YBCO+4BZO/Metal and YBCO/Metal samples. At a given field, the undoped YBCO/Metal sample exhibits a consistently higher peak compared to the BZO-doped sample, indicating stronger dissipation due to weaker flux pinning. The reduced peak height in the YBCO+4BZO/Metal sample confirms that BZO doping enhances flux pinning. As we can see from Figure 21(b), anomaly peak time has a non-uniform behavior with the magnetic field. The peak time for the YBCO/Metal sample has lower

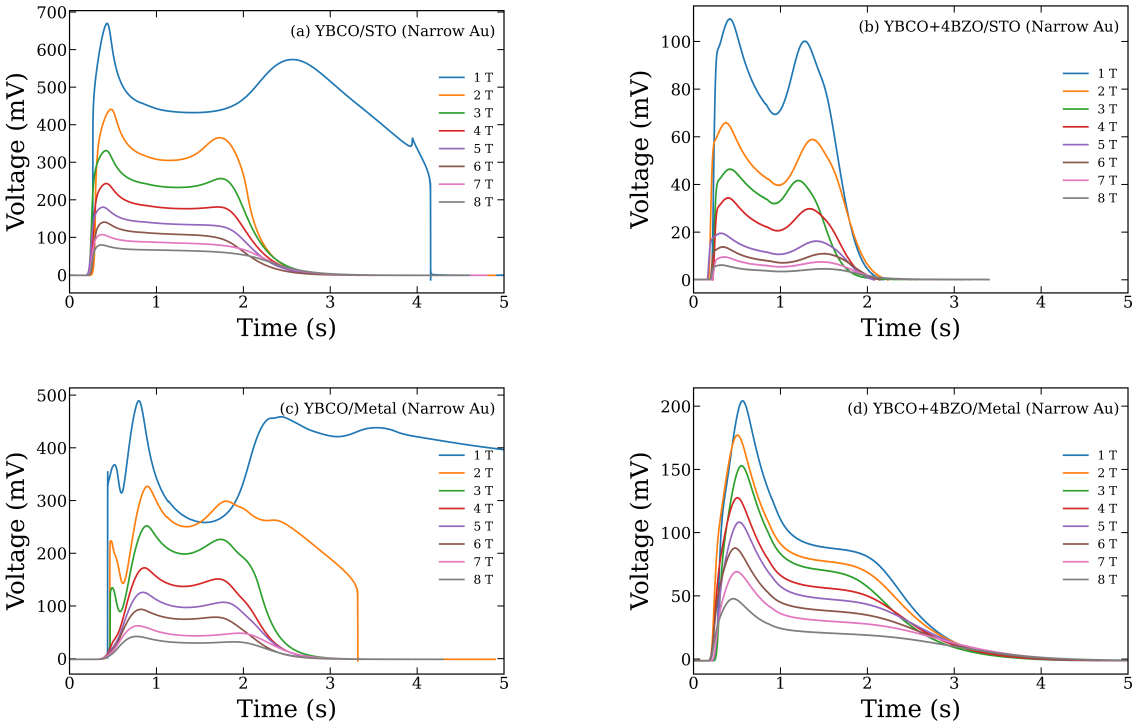

Figure 22: Magnetic field dependence of the quench behavior in small amount of Au-capped films. Each panel shows measurements at different magnetic fields from 0 to 8 T, highlighting the variation in quench dynamics and the emergence of anomaly.

values only at 0 T, while for the rest of the range it remains higher compared to YBCO+4BZO/Metal. As the magnetic field increases, the peak time varies slightly, yet it remains relatively high. On the other hand, for the YBCO+4BZO/Metal, the peak time has lower values and moderate fluctuations in the range of the applied field. This implies that the vortex relaxation process occurs quickly, which may indicate a stable state due to improved pinning.

3.4.4 Quench anomaly in films with narrow Au coating

In this section, we examine the quench behavior of the films that contain a small amount of Au capping. The following are the voltage-time graphs for different values of magnetic fields, which range from 0 to 8 T.

As in the previous case with wide Au capping, it is seen that the quench peak

appears immediately after the heat pulse, and then the anomaly peak appears. In case of YBCO/STO and YBCO+4BZO/STO, the response of the voltage is relatively well-defined, although compared to the widely Au-capped case, the peaks tend to be sharper, and have high voltage values. As shown in Figure 22(a), strong quench peak can be seen at low magnetic fields in the YBCO/STO sample. After this, a well-defined anomaly peak can be observed following a certain time delay, which corresponds to the process of relaxation. There is a noticeable difference between the quench peak and the anomaly peak and as the value of the magnetic field is increased, the heights of the peaks decrease. Also, at a higher value of the magnetic field, the anomaly peak is not clearly observed but is seen as a shoulder on the decaying voltage curve.

In the case of the YBCO+4BZO/STO sample, the overall voltage response is more controlled, and the voltage values are very small in comparison to the YBCO/STO. Moreover, there is decrease in the peak height, as well as less pronounced anomaly peak, which again verifies that an increase in flux pinning results in a suppression of vortex motion and a stabilization of superconductivity. The decrease in Au coverage results in a lesser effect of thermal spreading and current redistribution, making the intrinsic behavior of vortex motion more pronounced.

As can be seen from Figure 22(c) and (d), the voltage response curve for metal-based samples is more complex with higher peaks, particularly at low magnetic fields. For YBCO/Metal, at low magnetic fields, there is a double quench peak followed by a broad anomaly peak. As the magnetic field is increased, the peaks become smoother, and their height decreases. The YBCO+4BZO/Metal sample shows a decrease in the heights of the peaks and a controlled voltage response. The anomaly peak is not well defined and can be seen as a shoulder on the decaying curve. This shows the effects of BZO doping, which enhanced the pinning of flux and hinder the motion of the vortices.

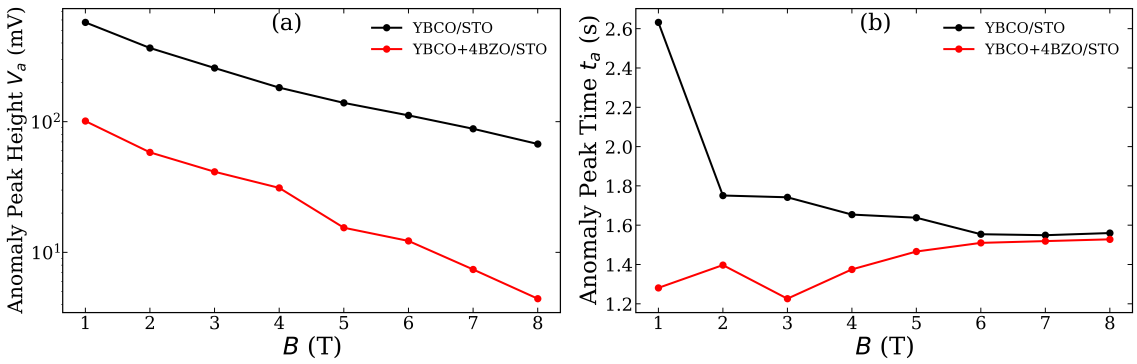

Figure 23: Magnetic field dependence of the anomaly peak height (a) and anomaly peak time (b) for YBCO/STO and YBCO+4BZO/STO films having a small amount of Au coating on them.

A clear dependence of the anomaly peak height and time is identified on the applied magnetic field for the STO-based samples as presented in Figure 23. The results show that the peak height decreases as the value of the magnetic field increases for both samples. The YBCO/STO sample has high peak heights, which suggests a high level of voltage and energy loss. Such results could be associated with poor flux pinning; on the other hand, this could also be attributed to the fact that the absolute currents in this sample are relatively high as compare to YBCO+4BZO/STO sample, that exhibits low peak heights in applied magnetic fields.

The anomaly peak time shows a non-uniform dependence on the magnetic field for the YBCO/STO and YBCO+4BZO/STO samples. In the YBCO/STO sample, the peak time shows a sharp increase at low magnetic field, a maximum at 1 T, then a gradual decrease and stabilization at higher magnetic fields. In the YBCO+4BZO/STO sample, the peak time shows lower values with minor fluctuations at the magnetic field range. With the increase of the magnetic field, the peak time shows a gradual increase, approaching the value of the YBCO/STO sample at higher magnetic fields.

Figure 24(a) clearly indicates that the height of the anomaly peak reduces sys-

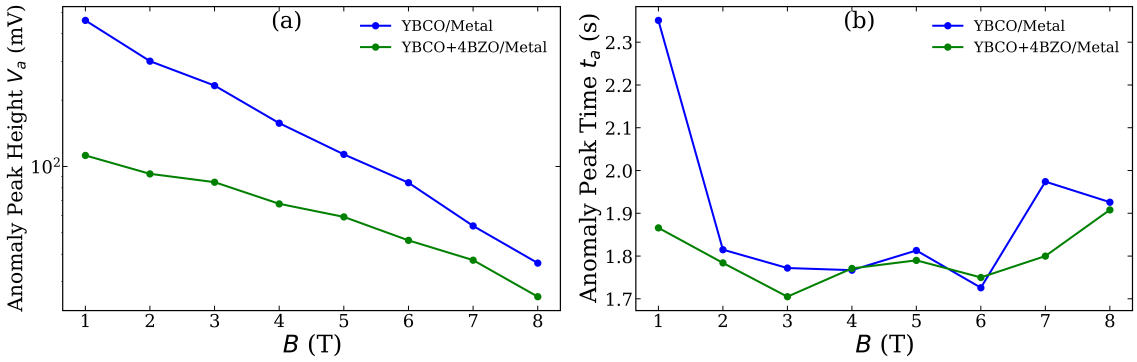

Figure 24: The anomaly peak height (a) and anomaly peak time (b) for YBCO/Metal and YBCO+4BZO/Metal films with a small amount of Au coating are depicted in these figures in relation to the magnetic field.

tematically with increasing magnetic field strength for both samples. The peak values for the YBCO/Metal sample are higher over the entire range of magnetic field strength, which is associated with relatively higher absolute current levels, which contribute to increased voltage response and energy dissipation, while the peak values for the YBCO+4BZO/Metal sample show a significant reduction. The difference between the two samples is more significant at low magnetic field strength, as indicated by the significantly higher peak values for the YBCO/Metal sample. With the increase of the magnetic field, the peak height decreases steadily in both samples. The decrease is steeper in the case of the YBCO/Metal sample, while the YBCO + 4BZO/Metal sample exhibits more gradual peak values across the applied magnetic field range.

The anomaly peak time indicates an irregular behavior with respect to the applied magnetic field for both YBCO/Metal and YBCO+4BZO/Metal. For sample YBCO/Metal, larger changes are observed with a sharp increase at low magnetic field and fluctuations at higher fields. For YBCO+4BZO/Metal, lower and smoother changes are observed over the applied magnetic field.

A comparison of wide and narrow Au-capped films indicates distinct differences

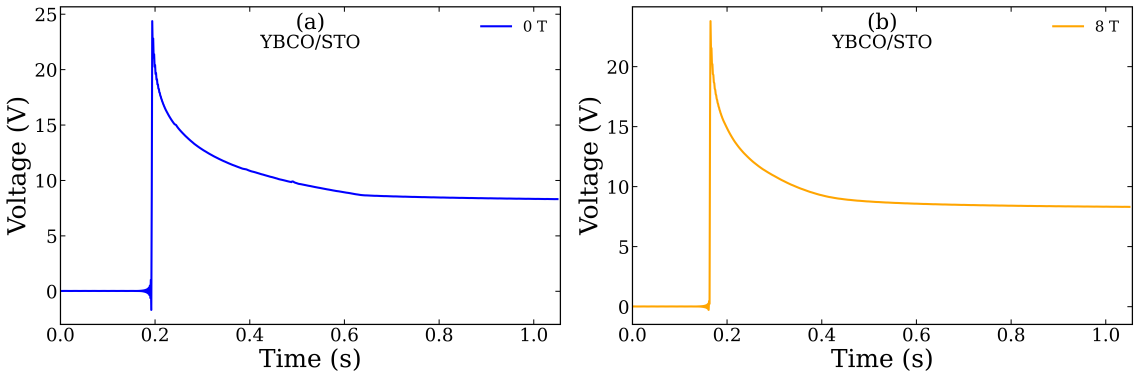

Figure 25: Voltage–time curves for YBCO/STO films without Au coating measured at two different magnetic fields 0 and 8 T.

in quench characteristics and anomaly peaks. Wide Au-capped films show smoother voltage responses with lower peak values and better thermal spreading characteristics due to maximum coverage with Au. In contrast, narrow Au-capped films show sharper voltage responses with higher peak values and lower thermal spreading characteristics. The peak height is seen to reduce significantly at higher values of the applied magnetic field in both wide and narrow Au cases.

3.4.5 Magnetic field dependence of quench and its anomaly in films without Au coating

Figure 25 illustrates the voltage-time characteristics of YBCO/STO films without Au coating, measured at two different magnetic fields, 0 T and 8 T. For both measurements, a sharp quench peak is observed, and then the voltage starts to decay.

In this case, the applied current was 85 mA at 0 T and 0.6 mA at 8 T. These values of currents are sufficiently high to induce quench, but there is no anomaly peak observed in either of these cases. The voltage signal is observed to have only a quench peak and a smooth decay. In the absence of Au coating, the voltage response is found to be highly localized, and the thermal spreading is found to be reduced. As a consequence, the quench peak is found to be very sharp. The

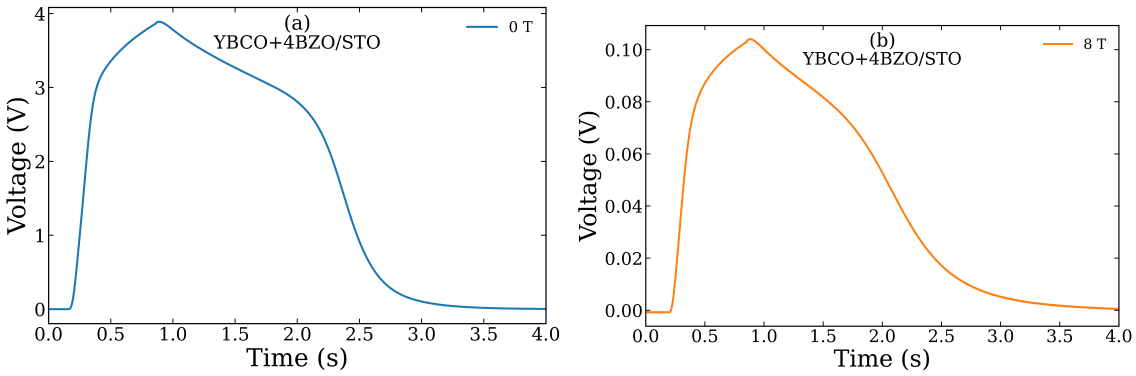

Figure 26: Voltage–time curves for YBCO+4BZO/STO films without Au coating measured at two different magnetic fields 0 and 8 T.

heat generated is found to be localized. Unlike the Au-coated cases, there is no appearance of a secondary peak. At 0 T, the peak is slightly higher, and at 8 T, the peak is slightly lower. Nevertheless, the voltage response is quite similar, and there is a small reduction in the peak height for 8 T.

The voltage-time plots of the YBCO+4BZO/STO films without the Au coating, measured at 0 T and 8 T, are depicted in Figure 26. In both plots, a quench peak is observed immediately after the heat pulse. In addition, a weak feature is observed subsequent to the quench peak, resulting in the anomaly-like shape. It is surprising that this feature is observed without the Au coating. In this particular case, the applied current was 12 mA at 0 T and 0.02 mA at 8 T. The low I_c values and the corresponding low applied currents may help to increase the sensitivity of the measurements, which allows the detection of this weak anomaly-like feature. This feature is less pronounced than in the Au-capped samples and looks more like a deviation from the smooth decay.

The weak anomaly-like feature is likely associated with the relatively low I_c values of the sample. Indeed, the low values of I_c make the system more sensitive to thermal changes, which enables the detection of subtle voltage features even in the absence of a well-defined anomaly peak. In contrast, the results reported in

the literature [46], particularly in Fig.3(b), exhibit a different response: a distinct and well-defined peak is observed for significantly higher I_c values. In those cases, the heat pulse produced a single well-defined quench peak in the voltage response without the appearance of any additional weak features.

In other words, it can be concluded that although the Au layer improves the intensity of the anomaly peak through thermal and current redistribution effects, there is a weak anomaly peak even without the presence of the Au layer, depending on the measurement conditions. However, this is observed with low values of I_c, and the exact reason is unknown.

3.4.6 Evolution of the quench anomaly peak along the stripe

Voltage–time responses were recorded at different locations along the stripe (Channels 1 to 4) to examine the propagation behavior of the normal zone, as shown in Figure 27 for the wide Au coated YBCO/STO sample measured at 1 T. From this observation, it can be noticed that the quench peak occurs first on Channel 1 and subsequently on Channels 2, 3, and 4 with a time delay. This time delay between these peaks indicates a phenomenon of propagation of a normal zone on a stripe. This delay between these channels directly indicates NZPV, which refers to the rate at which a resistive region propagates through a superconducting material.

In addition to the quench peak, the anomaly peak also decreases along the stripe. The anomaly peak is the strongest near Channel 1 and decreases in strength as it extends towards Channels 3 and 4. This reduction in peak strength indicates that the energy contained in the anomaly peak decreases along the stripe. This is because the current redistributes.

The peak voltages broaden and diminish with increasing distance, indicating the spreading and weakening of the resistive region during propagation. Similar behavior was observed in all samples, confirming that this is a general characteristic

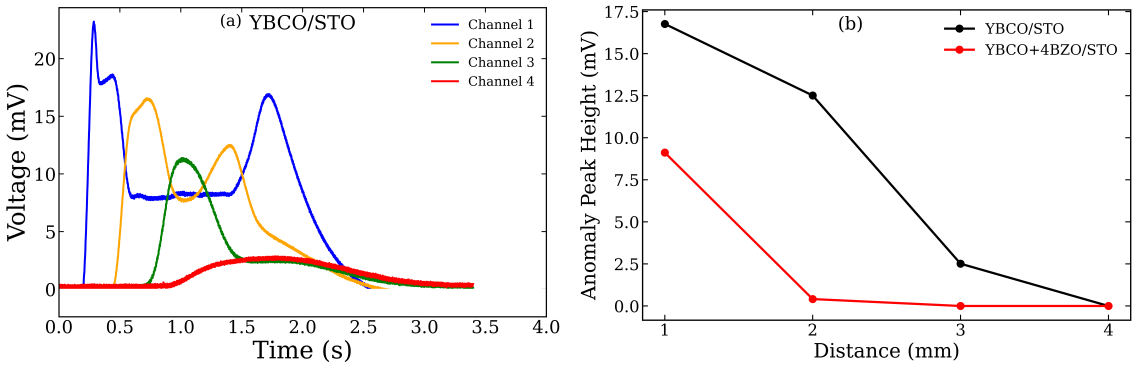

Figure 27: (a) Time evolution of quench and anomaly peaks along the YBCO/STO stripe with wide Au coating measured at 65 K and 1 T (channels 1–4, spaced by 1 mm). (b) Anomaly peak height as a function of position along the stripe.

of the system.

Figure 27(b) shows the variation of the anomaly peak height with distance along the stripe. For both YBCO/STO and YBCO+4BZO/STO samples, peak height decreases continuously with increasing distance from the initial quench point, with the highest peak observed at Channel 1 and gradual reduction up to Channel 4.

This shows that the energy associated with the anomaly is dissipated along the propagation path by the redistribution and relaxation of the current. The faster reduction in peak height for YBCO+4BZO/STO further supports the effect of improved flux pinning, which reduces the anomaly by inhibiting the movement of vortices.

3.5 Possible mechanisms behind quench anomaly

The quench measurements revealed a delayed second voltage peak that appears after the main thermally induced quench peak. As this anomaly is produced after the termination of the heating pulse and sometimes after partial restoration of the superconducting state, the phenomenon can not be described using the conventional thermal quench models. This indicates that an additional mechanism involving

non-equilibrium vortex dynamics, flux-pinning-dependent relaxation, and current redistribution must be considered.

The primary voltage spike is due to the heat input caused by the resistor pulse. The heat will lead to an increase in the local temperature of the superconducting strip. This causes a decrease in the critical current density in that area. Since the current density is near the critical value, the localized area enters the resistive state, initiating a quench [47]. This process leads to the formation of the primary voltage peak observed immediately after the heat pulse.

On the other hand, the delayed anomaly occurs after the occurrence of the quench and stays despite the absence of the thermal pulse. Such behavior indicates that the superconductor does not achieve stability right away, but rather evolves through a time-dependent recovery process before reaching equilibrium [48]. During the heat pulse, a localized region of the YBCO layer becomes resistive, forcing the transport current to transfer into the metallic stabilizer (Au). This current transfer occurs over a finite distance known as the current transfer length due to the presence of interfacial resistance between the superconductor and stabilizer [49]. Within this region, current sharing leads to Joule dissipation both in the stabilizer and across the interface. After removing the heat pulse, the temperature falls and the YBCO film starts regaining its superconductivity. But the current flow does not immediately come back to the superconducting layer. The back-transfer of current from the stabilizer to YBCO is delayed due to the same interfacial resistance [4, 49]. This might cause further Joule heating at the interface during the recovery stage, leading to the formation of a secondary peak in the voltage signal.

The role of the stabilizer thickness also plays a vital role as it has been observed that increasing stabilizer thickness significantly affects quench and recovery dynamics [50]. A thicker stabilizer allows a larger fraction of the current to flow in the metallic layer during a quench. Therefore, a greater current will have to return to

the superconducting film during the recovery process, resulting in higher interface dissipation. This phenomenon is more pronounced in samples where the Au layer is wider. This is further supported by [4], which demonstrates that interfacial resistance governs both normal zone propagation and stability in coated conductors. The delayed current redistribution during recovery can therefore be interpreted as a transient non-equilibrium state, characterized by incomplete and spatially non-uniform restoration of superconductivity. Apart from the existing redistribution, flux pinning also becomes important in this regard. In the undoped YBCO sample, flux pinning is weak, allowing vortex movement for dissipation through recovery. However, in the BZO-doped sample, there is strong flux pinning that prevents vortex movement. Similarly, increasing magnetic field modifies vortex dynamics, contributing to the observed reduction of the anomaly at higher fields. Overall, the quench anomaly arises from a coupled mechanism involving delayed current redistribution across the Au/YBCO interface, stabilizer-dependent current sharing, interfacial Joule heating during recovery and vortex relaxation processes governed by flux pinning [4, 49, 50].

4 Summary and conclusion

This thesis investigated the flux-pinning-dependent quench anomaly in Au-capped YBCO thin films. The major aim was to investigate the reason for the existence of the secondary voltage peak after the quenching event and its dependence on flux pinning, substrate, magnetic field strength, and Au capping.

Four YBCO thin film samples were studied: YBCO/STO, YBCO+4BZO/STO, YBCO/Metal, and YBCO+4BZO/Metal. The samples were prepared via pulsed laser deposition and patterned in stripe geometry through photolithography techniques, and was narrowly and widely coated with Au by e-beam evaporation. It was found that the films formed on STO substrates were more crystalline and exhibited sharper diffraction peaks, lower mosaic spread, and lesser strain than those

films formed on metal substrates. The metal-based films exhibited wider peaks and higher degrees of misorientation, signifying poor epitaxy. The incorporation of BZO induced extra strain but also generated artificial pinning sites, which significantly influenced both superconductivity and quenching.

In AC susceptibility measurements, it is seen that the imaginary susceptibility peaks shift towards lower temperatures with an increase in the magnetic field, suggesting suppression of the superconducting state by applying an external magnetic field. Doped samples with BZO exhibited sharper responses under magnetic fields than pure samples. In addition, critical current measurements revealed that both I_c and J_c were decreased as a function of increased magnetic field. When the temperature was low and the magnetic field was high, BZO doping resulted in better current behavior due to improved pinning; however, at 65 K, the effect of BZO doping was relatively modest.

The quench measurements were performed at 65 K using an operating current of 80% of the field-dependent critical current. The heat pulse was generated by using a resistor that was connected to the stripe. The voltage behavior for all the samples with Au coating had two important characteristics: firstly, a quench peak generated due to heat pulse, followed by a secondary peak occurring after the quench peak. This anomaly peak was very sensitive to flux pinning landscape. For the undoped samples, the anomalies were larger, suggesting vortex motion being stronger, resulting in more energy dissipation. But it is important to note that the undoped samples have a larger value of I_c, meaning that higher operating currents (80% of I_c) can be attained, giving rise to higher voltages. Therefore, the increased anomaly peak height in undoped samples may arise from a combined effect of weaker flux pinning and higher transport current. In this regard, it is possible to say that the high value of the anomaly peak can be due to a combined effect of weak flux pinning and higher transport current.

The effect of Au cap layer had a considerable impact on the resulting quenching behavior. The widely Au capped samples showed less fluctuation in their voltage behavior, while narrowly Au capped samples revealed sharp voltages peaks, signifying more heat accumulation and less thermal stabilization. In the absence of Au coating on samples, the anomaly was not detected or barely noticeable. This indicates that the Au film increases the detection of the anomaly through redistribution of current and thermal interaction.

From the voltage–time responses along the stripe, it can be observed that the quench peak appears first near the heater and then reaches subsequent voltage channels with a delay, indicating normal-zone propagation. The amplitude of the anomaly peak reduces with increasing distance from the original quench point.

Use of AI in thesis

While preparing this work, the use of some AI tools, particularly ChatGPT, was made to enhance my understanding of some concepts in academic papers and articles and to improve the readability and grammatical structure of some passages in English. Also, artificial intelligence assistance was provided to aid in programming using Python, especially in data analysis and graphing. Suggestions provided by the AI were thoroughly checked, corrected where need be, and incorporated into my work.

References

[1] D. Sibanda, S. T. Oyinbo, T.-C. Jen ja A. I. Ibitoye, Processes **10**, 1184 (2022) doi:10.3390/pr10061184.

[2] S. R. Foltyn, L. Civale, J. L. MacManus-Driscoll, Q. X. Jia, B. Maiorov, H. Wang ja M. Maley, Nat. Mater. **6**, 631 (2007) doi:10.1038/nmat1989.

[3] J. Huang ja H. Wang, Superconductor Science and Technology **30**, 114004 (2017) doi:10.1088/1361-6668/aa8d32.

[4] G. A. Levin, P. N. Barnes, J. P. Rodriguez, J. A. Connors ja J. S. Bulmer, IEEE Transactions on Applied Superconductivity **19**, 2504 (2009) doi:10.1109/TASC.2009.2019604.

[5] X. Wang, A. Caruso, M. Breschi, G. Zhang, U. Trociewitz, H. Weijers ja J. Schwartz, IEEE T. Appl. Supercond. **15**, 2586 (2005) doi:10.1109/TASC.2005.847661.

[6] H. K. Onnes, Commun. Phys. Lab. Univ. Leiden **12**, 120 (1911) doi:10.1038/086419a0.

[7] S. Nishijima, S. Eckroad, A. Marian, K. Choi, W. S. Kim, M. Terai, Z. Deng, J. Zheng, J. Wang, K. Umemoto, J. Du, P. Febvre, S. Keenan, O. Mukhanov, L. D. Cooley, C. P. Foley, W. V. Hassenzahl ja M. Izumi, Supercond. Sci. Technol. **26**, 113001 (2013) doi:10.1088/0953-2048/26/11/113001.

[8] V. Z. Kresin ja S. A. Wolf, *Fundamentals of Superconductivity* (SpringerNew York, 2013) doi:10.1007/978-1-4899-2507-7.

[9] W. Meissner ja R. Ochsenfeld, Naturwissenschaften **21**, 787 (1933) doi:10.1007/bf01504252.

[10] M. Hasan, R. Dong, H. J. Choi, D. S. Lee, D.-J. Seong, M. B. Pyun ja H. Hwang, Applied Physics Letters **92**, 202102 (2008) doi:10.1063/1.2932148.

[11] F. London ja H. London, Proceedings of the Royal Society of London. Series A-Mathematical and Physical Sciences **149**, 71 (1935) doi:10.1098/rspa.1935.0048.

[12] V. L. Ginzburg ja L. D. Landau, *On Superconductivity and Superfluidity: A Scientific Autobiography* (SpringerBerlin, Heidelberg, 2009), pp. 113–137 doi:10.1007/978-3-540-68008-6_9.

[13] J. Bardeen, L. N. Cooper ja J. R. Schrieffer, Physical Review **108**, 1175 (1957) doi:10.1103/physrev.108.1175.

[14] J. G. Bednorz ja K. A. Müller, Z. Phys. B **64**, 189 (1986) doi:10.1007/978-94-011-1622-0_32.

[15] M. K. Wu, J. R. Ashburn, C. J. Torng, P. H. Hor, R. L. Meng, L. Gao, Z. J. Huang, Y. Q. Wang ja C. W. Chu, Phys. Rev. Lett. **58**, 908 (1987) doi:10.1103/physrevlett.58.908.

[16] M. D. Ainslie, Transport AC Loss in High Temperature Superconducting Coils, 2012.

[17] Z. Lian, Z. Pingxiang, J. Ping, W. Keguang, W. Jingrong ja W. Xiaozu, Superconductor Science and Technology **3**, 490 (1990) doi:10.1088/0953-2048/3/10/002.

[18] A. Goyal, R. Kumar, H. Yuan, N. Hamada, A. Galluzzi ja M. Polichetti, Nature Communications **15**, 6523 (2024) doi:10.1038/s41467-024-50838-4.

[19] M. M. Aye, E. Rivasto, H. Rijckaert, S. Granroth, H. Palonen, H. Huhtinen, I. V. Driessche ja P. Paturi, ACS Applied Nano Materials **5**, 18159 (2022) doi:10.1021/acsanm.2c04054.

[20] Z. Li, M. Coll, B. Mundet, N. Chamorro, F. Vallès, A. Palau, J. Gazquez, S. Ricart, T. Puig ja X. Obradors, Scientific reports **9**, 5828 (2019) doi:10.1038/s41598-019-42291-x.

[21] J. Wu, M. Panth, V. Ogunjimi, B. Gautam, J. Shi, M. A. Sebastian, T. Haugan, C. Ebbing, D. Zhang, J. Jian *et al.*, IEEE Transactions on Applied Superconductivity **33**, 3254489:1 (2023) doi:10.1109/tasc.2023.3254489.

[22] M. Marchevsky, Instruments **5**, 27 (2021) doi:10.3390/instruments5030027.

[23] J. D. Weiss, R. Teyber, M. Marchevsky ja D. Van Der Laan, Superconductor Science and Technology **33**, 105011 (2020) doi:10.1088/1361-6668/abaec2.

[24] J. Schwartz, Quench in high temperature superconductor magnets, 2014.

[25] Y. Wu, W. Song ja M. Yazdani-Asrami, Superconductivity **14**, 100173 (2025) doi:10.1016/j.supcon.2025.100173.

[26] E. E. Salazar, R. A. Badcock, M. Bajko, B. Castaldo, M. Davies, J. Estrada, V. Fry, J. T. Gonzales, P. C. Michael, M. Segal *et al.*, Superconductor Science and Technology **34**, 035027 (2021) doi:10.1088/1361-6668/abdba8.

[27] E. Ravaioli, V. Datskov, G. Kirby, H. Ten Kate ja A. Verweij, Superconductor Science and Technology **27**, 044023 (2014) doi:10.1088/0953-2048/27/4/044023.

[28] P. R. Willmott ja J. R. Huber, Reviews of Modern Physics **72**, 315 (2000) doi:10.1103/RevModPhys.72.315.

[29] C. Ma ja C. Chen, *Pulsed Laser Deposition of Thin Films: Applications-Led Growth of Functional Materials* (Wiley-VCH Verlag GmbH & Co. KGaAWeinheim, Germany, 2016), luku 1 doi:10.1002/9783527696406.ch1.

[30] R. Eason, *Pulsed Laser Deposition of Thin Films: Applications-Led Growth of Functional Materials* (John Wiley & SonsChichester, United Kingdom, 2007).

[31] C. Popescu, G. Dorcioman ja A. C. Popescu, *Laser Ablation* (IntechOpenLondon, United Kingdom, 2016) doi:10.5772/65124.

[32] B. D. Cullity ja S. R. Stock, *Elements of X-Ray Diffraction*, 3 ed. (Prentice HallUpper Saddle River, New Jersey, 2001) doi:10.1063/1.3060306.

[33] G. F. Harrington ja J. Santiso, Journal of Electroceramics **47**, 141 (2021) doi:10.1007/s10832-021-00263-6.

[34] K. Buchkov, A. Galluzzi, E. Nazarova ja M. Polichetti, Materials **16**, 4896 (2023) doi:10.3390/ma16144896.

[35] M. J. Madou, *Fundamentals of Microfabrication: The Science of Miniaturization*, 2 ed. (CRC PressBoca Raton, Florida, 2018) doi:10.1201/9781482274004.

[36] S. Wang, Z. Zhou, B. Li, C. Wang ja Q. Liu, Materials Today Nano **16**, 100142 (2021) doi:10.1016/j.mtnano.2021.100142.

[37] J. Merkel, T. Sontheimer, B. Rech ja C. Becker, Journal of Crystal Growth **367**, 126 (2013) doi:10.1016/j.jcrysgro.2012.12.037.

[38] T. Hirvikorpi, M. Vähä-Nissi, A. Harlin ja M. Karppinen, Thin Solid Films **518**, 5463 (2010) doi:10.1016/j.tsf.2010.04.018.

[39] R. K. Sharme, M. Quijada, M. Terrones ja M. M. Rana, Materials **17**, 4559 (2024) doi:10.3390/ma17184559.

[40] J. Ye ja K. Nakamura, Physical Review B **48**, 7554 (1993) doi:10.1103/physrevb.48.7554.

[41] A. Galluzzi, A. Crisan, A. M. Ionescu, I. Ivan, A. Leo, G. Grimaldi ja M. Polichetti, Applied Sciences **14**, 4379 (2024) doi:10.3390/app14114379.

[42] Z.-X. Ye, Q. Li, Y. Hu, W. Si, P. Johnson ja Y. Zhu, Applied Physics Letters **87**, 122502 (2005) doi:10.1063/1.2051794.

[43] E. Bartolomé, A. Palau, A. Llordés, T. Puig ja X. Obradors, Phys. Rev. B **81**, 184530 (2010) doi:10.1103/physrevb.81.184530.

[44] J. Zhang, H. Wu, G. Zhao, L. Han ja J. Zhang, Nanomaterials **12**, 4000:1 (2022) doi:10.3390/nano12224000.

[45] T. Vaimala, M. Aye, E. Rivasto, Y. Zhao, H. Huhtinen ja P. Paturi, Physica C: Superconductivity and its applications **624**, 1354565 (2024) doi:10.1016/j.physc.2024.1354565.

[46] S. Mejia, M. M. Aye, H. Huhtinen ja P. Paturi, Superconductor Science and Technology **38**, 105008 (2025) doi:10.1088/1361-6668/ae0dbe.

[47] D. Golubev, F. Lombardi ja T. Bauch, Physica C: Superconductivity and its Applications **506**, 174 (2014) doi:10.1016/j.physc.2014.06.013.

[48] F. S. Wells, A. V. Pan, I. A. Golovchanskiy, S. A. Fedoseev ja A. Rozenfeld, Scientific Reports **7**, 40235 (2017) doi:10.1038/srep40235.

[49] G. A. Levin, K. A. Novak ja P. N. Barnes, Superconductor Science and Technology **23**, 014021 (2009) doi:10.1088/0953-2048/23/1/014021.

[50] N. Y. Kwon, H. S. Kim, K. L. Kim, S. Hahn, H.-R. Kim, O.-B. Hyun, H. M. Kim, W. S. Kim, C. Park ja H. G. Lee, IEEE Transactions on Applied Superconductivity **20**, 1246 (2010) doi:10.1109/tasc.2009.2039864.